Coastal Carolina University

CCU Digital Commons

Electronic Theses and Dissertations   College of Graduate Studies and Research

4-30-2020

The Effect of Radium Partitioning on Hydrothermal Fluid Flow Determination across Guaymas Basin

Charlotte R. Kollman
Coastal Carolina University

Follow this and additional works at: https://digitalcommons.coastal.edu/etd

Part of the Oceanography Commons

Recommended Citation

The Effect of Radium Partitioning on Hydrothermal Fluid Flow Determination across Guaymas Basin

By
Charlotte R. Kollman

_____

Submitted in Partial Fulfillment of the Requirements for the Degree of Master of Science
in Coastal Marine and Wetland Studies in the School of the Coastal Environment
Gupta College of Science
Coastal Carolina University
May 2020

_____   _____
Dr. Richard Peterson   Dr. Andreas Teske
Major Professor   Committee Member

_____   _____
Dr. Richard Viso   Dr. Richard Peterson
Committee Member   Major Professor
Chair, Department of Coastal
Marine Systems Science

                                                _____
                                                Dr. Michael Roberts
                                                Dean, Gupta College
_____   of Science
Dr. Angelos Hannides
Major Professor

Abstract

Analysis of the distribution of radium through sedimentary porewater profiles is a promising method for constraining diffuse discharge/recharge flow rates in hydrothermal settings; these parameters are critical for evaluating hydrothermal circulation and its chemical and biological implications. The short-lived ^{224}Ra (T1/2 = 3.54 days) is an effective tracer due to its behavior in marine environments and changes in activity due to ingrowth/decay. However, the distribution of radium may be influenced by its varying solid:aqueous partitioning coefficients (K_d) and is critical to understand for any study utilizing radium as a tracer. This project explores K_d across the hydrothermally active Guaymas Basin in the Gulf of California to understand the potential influence of partitioning by various environmental conditions, such as the rate of flow through hydrothermal sediments. A secondary goal of this project was to detect a measurable radium signature within the water column over areas of hydrothermal venting, such that this tracer may ultimately be useful to constrain mixing of the hydrothermal plume with ambient waters. Sixteen sediment cores across the southern basin were collected on cruise AT42-05 in November 2018, using HOV *Alvin.* Differing flow conditions were targeted in background sediments, areas of suspected diffuse flow marked by microbial mats, and areas of visual discharge. Porewater from cores sectioned in 4 cm intervals was analyzed for ^{224}Ra. Sediments were then returned to the lab for K_d analysis. We compare measured K_d values across the basin for statistically significant relationships between partitioning, biological sediment overgrowth, and porewater temperature. We also employ a vertical exchange model that utilizes the gradient of ^{224}Ra through porewater to estimate flow conditions (direction and magnitude) and couple K_d with our rate estimates to examine the

effect of partitioning on studies using radium as a tracer of fluid flux. Our results conclude only 4% of the variation in radium partitioning across the basin is attributed to venting site. We also found no correlation between effective fluid flux measurements and K_d. Distributions in K_d seem to be controlled by sediment heterogeneity in this setting, and are not necessary for calculating flux estimates via ^{224}Ra isotopes through hydrothermal sediments in Guaymas Basin. Initial results to constrain hydrothermal plumes were promising, and additional sample collection/analysis is certainly warranted to better understand the potential of utilizing ^{224}Ra as tracer of dispersed, ambient plume water into the surrounding ocean.

Table of Contents

List of Tables

List of Figures

1. Introduction and Background

In mid-ocean ridge spreading centers (MORs), hydrothermal vents inject superheated geologic fluid into the water column[1]. Hydrothermal fluid is formed from cold, bottom water that subducts into the crust through density-driven recharge (Alt, 1995). Typically, this water then becomes superheated by nearby magma chambers associated with the tectonic spreading centers and becomes enriched in reduced metals through high-temperature water-rock interactions (Figure 1). In most hydrothermal systems, as the water heats, it becomes buoyant and ascends through geologic fractures before escaping through vents in the seafloor (Stein et al., 1995). These vents can form large structures as these metals chemically precipitate upon contact with the cold, oxic water column. Deposition of these precipitates can form solid structures called "chimneys" or be carried via benthic currents and create plumes called "smokers" (German and Von Damm, 2003).

Hydrothermal chimneys deposit near areas of focused venting. These physical structures are the result of metals and sulfides that precipitate out from the superheated fluid. Tivey (1998) describes the chemical composition of chimneys as a base of anhydrite ($CaSO_4$) which builds quickly (i.e., several cm/day) from the venting fluid as a result of the calcium-rich vent fluid mixing with sulfates in the water column. Metal sulfide compounds of iron and copper then precipitate out and build along the inner wall of the anhydrite (Tivey, 1998). Venting chimneys in some other hydrothermal systems are built up from a discharging mixture of metal sulfides, calcite, and silicate (Peter and Scott, 1988).

---

[1] First described in 1977 in the Galapagos Rift (Lonsdale, 1977; Corliss and Ballard, 1977; Ballard, 1977).

In other areas with no visible chimneys, slower flow (i.e., seepage) may exist through cracks and fissures around the vents, providing another conduit for hydrothermal fluids to escape into the water column (Tivey, 2007). Such seepage processes often occur farther off-axis from the active chimney venting, where discharging fluid is less heated and discharge pathways are more sporadic (Stein and Stein, 1994; Santos et al., 2011). Although seepage is often more diffuse than focused flow through chimneys, wide dissemination of the seeps through hydrothermal sediments fosters diverse macro and microorganisms and can have a profound impact on the ecology surrounding these systems (Lonsdale and Becker, 1985; Childress and Fisher, 1992; Stein and Stein, 1994). This diffused venting is therefore a vital component at active spreading centers for its role in hydrothermal ecosystems.

Active hydrothermal areas contain communities of rich biological diversity (Lonsdale, 1977; Corliss et al., 1979; Grassle, 1983). Discharging fluid from focused venting and off-axis diffuse seepage provides carbon and energy sources to support diverse chemosynthetic ecosystems in these benthic habitats (Jannasch, 1983; Jannasch, 1995; Takai and Nakamura, 2010; Bris et al., 2016; Portail et al., 2016). Hydrothermal fluid is typically acidic, anoxic, and laden with hydrocarbon gases and metals (Campbell et al., 1994; Von Damm, 1995; Kadko, 1996). Thiotrophs and methanotrophs at active seep sites consume sulfide and methane within the discharging fluid. These microbes, in turn, support wider benthic assemblages around the seeps (Jannasch, 1983; Takai and Nakamura, 2010; Bris et al., 2016; Portail et al., 2016).

One area with diffused hydrothermal venting, extensive sediment coverage, and bacterial mat growth is Guaymas Basin in the Gulf of California (Lonsdale, 1978; Lonsdale

et al., 1980; Campbell and Gieskes, 1984). In Guaymas Basin, hydrothermal circulation differs from other systems, due to the thick sediment coverage. Instead, shallow fluid circulation occurs through basaltic sill intrusions while deep-fluid circulation flows through fault zones, where sills act as a type of "cap rock" (re: Fig. 1; Einsele et al., 1980; Gieskes et al., 1982; Kastner, M., 1982). Guaymas Basin is an excellent site to study the interaction between hydrothermal flow and microbial mat growth due to diverse discharge conditions and organisms found in close proximity to each other, supporting entire chemosynthetic ecosystems that develop around the vents and seeps (Lonsdale and Becker, 1985; Portail et al., 2015; Portail et al., 2016; Teske et al., 2016). Large-scale pelagic and terrigenous sediment coverage, hundreds of meters to 1 km thick in some areas, (Calvert, 1966; Lonsdale and Becker, 1985) has a profound effect on the volcanism and hydrothermal activity in the basin. The abundant, widespread sediment coverage disseminates hydrothermal fluid through the sediments more evenly, unlike the typical patchy discharge patterns at other spreading centers where sediment coverage is not as thick or extensive (Lizarralde et al., 2007).

Chemosynthetic bacteria comprise the base of the food chain among hydrothermal ecosystems and are abundant in Guaymas Basin due to its widespread sedimentation and the chemistry of the discharging endmember fluid (Jannasch, 1983). One such notable bacteria, *Beggiatoa* spp., a marine strain of the *Beggiatoaceae* family (Teske and Salman, 2014) is a large (visible) organism that forms microbial mats on benthic surfaces near submarine seep and vent sites (Nelson et al., 1989; Gundersen et al., 1992; Teske et al., 2014). These bacteria are filamentous autotrophs that oxidize the sulfur-rich vent fluids via denitrification and use the energy derived from this oxidation to fuel their metabolism

(Nelson and Jannasch, 1983; McKay, et al., 2012; Teske and Salman, 2014). *Beggiatoa* spp. then assimilate CO_2 in the discharging fluid and support biological activity on the seafloor (Nelson and Jannasch, 1983; McKay, et al., 2012; Teske and Salman, 2014; Schutte et al., 2018). *Beggiatoa* spp. are well suited to thrive in areas of high sedimentation. The sediment diffuses hydrothermal seep flows, distributing the heated fluid across a wider surface area and allowing for more extensive bacterial growth (McKay et al., 2012).

However, a central aspect of hydrothermal systems like Guaymas Basin that remains largely unquantified is the range of flow rates of hydrothermal seepage (and therefore supply rate of biogeochemical solutes needed to support the chemosynthetic communities) across the sediment-water interface (Levin et al., 2016). Such flow can impact microbial and biological assemblage growth rates and distribution, as well as biogeochemical solute cycling into the surrounding ocean, yet slow (diffuse) flow rates are often difficult to quantify. Additionally, water flow can occur bidirectionally across the sediment-water interface. Upward flow through the sediments can supply benthic and sedimentary communities with reduced compounds critical to their chemosynthetic metabolisms. Downward flow can also impact benthic communities by carrying oxygen and other nutrients into highly reducing sediments.

Scientists often rely on one-dimensional advection-diffusion models to estimate hydrothermal flow rates through shallow sediments. Heat (thermal) profiles and geochemically conservative chemical tracers that may be enriched in hydrothermal waters have been used as model parameters to characterize localized advection dynamics (Berner, 1980; Von Damm et al., 1985). However, successful application of these methods has traditionally been limited to areas where flow conditions are sufficiently elevated that

distinct differences in flow proxies can be detected, but gradients in these parameters are not always measurable under hydrothermal seepage conditions. Therefore, the argument has been made for a method that does not rely on the existence of a heat or salt gradient in order to expand the environmental conditions in which porewater flow rates may be estimated (Peterson, 2019).

Radium isotopes have long been recognized for their utility in tracing various marine processes. The suite of four naturally-occurring isotopes, ^{223}Ra, ^{224}Ra, ^{226}Ra, and ^{228}Ra, has been instrumental in characterizing submarine groundwater discharge (SGD) locations and rates, modeling interface diffusional processes, and tracing aspects of ocean circulation, estuarine mixing, and bioturbation (e.g., Moore, 1997; Krest et al., 2000; Burnett et al., 2002; Krest and Harvey, 2003; Peterson et al., 2008). The range in half-lives (^{223}Ra = 11.4 days, ^{224}Ra = 3.66 days, ^{226}Ra = 1600 years, and ^{228}Ra = 5.7 years) makes this suite of isotopes an efficient tracer option across a wide range of time scales. In particular, the brief half-life of ^{224}Ra makes that isotope especially useful for studying short-term processes (e.g., Rama and Moore, 1996; Charette et al., 2001; Moore et al., 2008).

Ra-224 is relatively soluble in saline environments due to ion exchange processes, unlike its highly particle-reactive ^{228}Th parent (Krishnaswami *et al.*, 1982). Ra-224 is formed from decay of its parent (^{228}Th), and in saline environments, some ^{224}Ra will desorb from particles and become dissolved in porewaters. After approximately 6 half-lives (22 days), ^{224}Ra activities in porewater effectively reach secular equilibrium whereby the rate of decay of the dissolved ^{224}Ra population will equal the rate of supply by the combined effects of ^{228}Th decay followed by desorption from the sediment surfaces into the porewater

(Fig. 3). Thereafter, dissolved ^{224}Ra activities should remain constant. This brief time frame makes the ^{224}Ra/^{228}Th relationship ideal for studying porewater flow through shallow sediments.

The radium partition coefficient is equal to the fraction of solid-sorbed exchangeable radium to dissolved exchangeable radium in solution (Krest and Harvey, 2003):

$$K_d = \frac{[Ra_{Adsorbed}]}{[Ra_{Dissolved}]} \qquad \text{(Eq. 1)}$$

In using a simplified, one-dimensional advection-dispersion model of porewater ^{224}Ra activities to estimate flow through shallow marsh sediments, Krest and Harvey (2003) assumed both K_d and the radium production rate to be constant. Yet, these authors highlight the need to understand the effect of radium partitioning in groundwater fluid recharge and discharge studies utilizing these isotopes. The distribution of radium isotopes may have a substantial impact on the pattern of observed radium within the porewater, and therefore any determined rates of recharge and discharge utilizing ^{224}Ra.

These behaviors of radium isotopic ingrowth/decay and solubility can be used in a vertical exchange model to calculate ^{224}Ra transport (and therefore water flow) through hydrothermal sediments (Peterson, 2019). This method is based on the ideas put forth by Krest and Harvey (2003). In the Peterson (2019) model, residence time of dissolved ^{224}Ra in discrete layers of the sediments is computed from changes of aqueous activity between adjoining sediment layers, utilizing the concepts of isotopic production and decay toward establishing secular equilibrium with each discrete sediment layer.

A primary assumption of the Peterson (2019) model is that K_d is vertically and spatially homogenous across Guaymas Basin. This assumption was based on a limited number of K_d measurements from which a representative value of K_d across Guaymas Basin was estimated. Without a broader data set of K_d values, assumptions of spatially uniform K_d across the study site led to flow rate estimates that were considered to represent conservative estimates. Any instantaneous changes in dissolved ^{224}Ra activity that may result from different K_d values are attributed to the slow ingrowth/decay process under homogenous K_d assumptions, which may over-estimate resident times and therefore underestimate flow velocity. Further exploration of the lateral and vertical variability in K_d values across Guaymas Basin will provide insight both into the effect of radium partitioning on fluid flow estimates through shallow sediments and any controls on K_d by environmental conditions.

The primary objective of this project is to explore ^{224}Ra K_d values and their distributions across Guaymas Basin to test the assumption (from Peterson, 2019) of uniform and homogeneous K_d values in this study site. We suspect that K_d is primarily a product of the geochemistry of the sediments. While some small-scale variability in sediment geochemistry is likely occurs across Guaymas Basin, the source of the sediments (largely pelagic, silica-rich deposits described by Calvert (1966) to represent over 50% of sediment deposition in the basin) that have been deposited in Guaymas Basin would be similar across the area. Therefore, we anticipate finding no systematic variation in K_d across Guaymas Basin. Additionally, we analyze the relationships between K_d, flow rate through the sediments, and bacterial mat composition to further characterize the K_d distribution across the basin. A final and tertiary objective of this study is to determine

whether measurable radium signatures are detectable within the water column over areas of hydrothermal venting, such that this tracer may ultimately be useful to constrain mixing of the hydrothermal plume with ambient waters.

2. Methods

2.1 Sediment Core Collection

Sixteen sediment push cores were collected using the human-occupied vehicle (*HOV) Alvin* during 11 dives in Guaymas Basin during a research cruise on-board the *R/V Atlantis* (AT42-05) in November 2018 (Table 1) from 3 distinct sampling sites: Aceto Balsamico, Mat Mound, and Cathedral Hill (sample site descriptions can are detailed in Teske et al., 2016). Prior to core collection, temperature profiles through the upper 50 cm of sediments were measured using a 0.6m Heatflow probe. Cores are identified throughout as 'Core 1-16' (complete sampling metadata can be found in Appendix I).

Five cores were collected in Aceto Balsamico on 3 different dives. One Aceto Balsamico core was collected directly through orange microbial mat, 1 core was collected in sediment under yellow microbial mat coverage, 2 were collected under white microbial mat coverage, and 1 was collected through brown, background sediment. In Mat Mound, 2 cores were collected on 1 dive, within and just outside of orange microbial mat coverage. The remaining 9 cores were collected in Cathedral Hill on 4 different dives. Two Cathedral Hill cores were collected through orange microbial mat cover, 1 was collected on the fringe edge outside of an orange microbial mat, 1 core was collected through yellow microbial

mat, 4 cores were collected through white microbial mat, and 1 core was collected through brown, background sediment (Appendix II).

Sediment cores from specific targets of interest were collected into 6.4 cm diameter core liners. Once on deck, cores were photographed and visually described based on length, composition, and microbial mat cover. Overlying water was siphoned off and preserved for Ra analysis. The cores were then sectioned at 4 cm intervals under an inert (argon) atmosphere into 50 mL centrifuge tubes. Small subsamples of sediment from each layer were sealed in pre-weighed glass vials from which porosity was measured in the lab by mass loss upon drying (Lambe, 1951). Following centrifugation of the samples at 5,000 rpm for 15 minutes, the supernatant water was recovered for immediate ^{224}Ra analysis and the remaining sediment was sealed to return to the laboratory for incubations (described in section 3.2 below).

Porewater volumes separated during centrifugation were filtered through 0.45 µm syringe filters, diluted with 1 L radium-free seawater, and slowly passed through 25 g of dry, acrylic fiber that has been impregnated with MnO_2 (Moore and Reid, 1973). This Mn fiber quantitatively sorbs Ra isotopes from the water (Moore, 1976; Moore, 2007). The process of passing the sample over the fiber twice enable maximum radium sorption to the fiber. The fibers were then rinsed with radium-free fresh water and dried to an appropriate humidity (as per Sun and Torgersen, 1998). Sample fibers were then measured on a Radium Delayed Coincidence Counter (RaDeCC) which analyzes ^{223}Ra and ^{224}Ra decay via alpha counting using a photomultiplier tube and large scintillation cell (Moore and Arnold, 1996). After ~21 days, fibers were recounted to correct for remaining ^{228}Th on the sample (Moore, 2008). Excess ^{224}Ra is used throughout this work and is collected as the difference

9

in ^{224}Ra activity between the initial count and that supported by ^{228}Th on the fiber during the second count.

2.2 Lab Incubation Methods

After returning from the cruise, average porosity and dry bulk density of each layer were measured from the subsamples collected in the sealed glass vials based on techniques outlined by Lamb (1951). Afterward, each sediment sample separated from its porewater via centrifugation was recovered from the centrifuge tubes and dried completely in a drying oven at 50°C. Based on the porosity and bulk density measurements for each sample, the dried sediment was then rehydrated with a volume of filtered, radium-free seawater to replicate in-situ porosity at the time of core collection. These hydrated sediments were then incubated in 1 L Nalgene bottles for 21-22 days to allow ^{224}Ra in porewater to grow into secular equilibrium with its solid-sorbed ^{228}Th parent. Over the course of the three-week incubations, the incubation bottles were regularly agitated to ensure particle saturation. At the conclusion of the incubation period, the same procedure as was used in the field (i.e. centrifugation, porewater filtering, passing over Mn fibers, and counting via a RaDeCC) was repeated to measure the dissolved radium in the incubation water.

2.3 Partition (K_d) Coeeficients

As previously mentioned, the resulting measurements of the incubation experiments are the end result of ^{224}Ra production via sedimentary ^{228}Th decay and desorption due to partitioning. K_d values were measured following the procedure from

10

Colbert and Hammond (2008). Dry sediment samples were hydrated with a defined volume of Ra-free seawater based on the water:sediment ratio (~85% water:sediment) in Colbert and Hammond (2008). After 24 hours, ~23% of the water volume was removed from the solution and replaced with Ra-free seawater. This removal/readdition process was repeated 4 times with 10 mintues between each step. With each removal, a portion of the dissolved ^{224}Ra is removed from the solution. Upon addition of Ra-free seawater, more ^{224}Ra is released from the sediments and is transferred into the aqueous phase as controlled by the partitional coefficient inherent to those sediments. Each volume of water removed was diluted with 1 L of Ra-free seawater and immeditely passed over a MnO_2 fiber and measured on the RaDeCC, following the same procedure as outlined above.

K$_d$ values were determined by the equation outlined in Colbert and Hammond (2008):

$$\frac{1}{M_s}(\Delta V \sum \lambda C_{i-1} + V_T \lambda C_i) = -K_d \lambda C_i + E$$

(Eq. 2)

where M_s is the mass of the aged sediment, E (the *y*-intercept) is the emanation rate of available ^{224}Ra ready to move into solution, V_T is the total porewater volume, ΔV is the volume of the aliquot removed, and λC_{i-1} is the sum of the activity of ^{224}Ra after each removal step. The total calculated ^{224}Ra activity sorbed to the sediments (*y*) and the measured activity of the ^{224}Ra in solution ($x, or \lambda C_i$) are plotted against each other, and K$_d$ is found to be the slope of the line, where the lowest aqueous activity measured at the end is associated with the maximum activity still sorbed to the sediments, as described in Equation 1.

For each removal step, a decrease in aquous activity should occur according to the principles of isotopic production and decay, leading to four values that are ultimately plotted and used to calculate K_d along a negative slope, following Eq.2. However, in the cases where K_d could not be calculated due to experimental error resulting in less than 4 realistic activities that decreased over the course of the experiment (resulting in a positive slope or one with an $R^2 < 0.9$), K_d was then determined by the equation outlined below:

$$\frac{X+\frac{(RaR-Ra1)}{Ms}}{\frac{Ra1}{\Delta V}} = \frac{X+\frac{(RaR-Ra1-Ra2)}{Ms}}{\frac{Ra2}{\Delta V}} = \frac{X+\frac{(RaR-Ra1-Ra2-Ra3)}{Ms}}{\frac{Ra3}{\Delta V}} = \frac{X+\frac{(RaR-Ra1-Ra2-Ra3-Ra4)}{Ms}}{\frac{Ra4}{\Delta V}} =$$

$$K_d \qquad\qquad\qquad\qquad\qquad\qquad\qquad (Eq.3)$$

where M_s is the mass of the sediment, X (or Ra_{final}) is the unknown amount of radium remaining in the bottle following the experiment, ΔV is the extracted volume in each step, variables $Ra_1, Ra_2, Ra_3,$ and Ra_4 are the measured activity removed from the bottles in each step, and Ra_R is the total activity removed following the completion of the experiment. Eq. 3 functionally works as a way to calculate a K_d value for each removal step rather than calculating it from the slope of the line in Eq. 2. Given that any part of the equation can substitute for another, we are able to omit steps where there was not a plausible decrease in activity due to experimental error. Therefore, in an example where the activity measured after step 2 was not less than the initial activity, we could measure the change from step 1 into step 3, but also 1 into 4, in order to make up for the missing data from step 2. The reported K_d for the core was collected as the average K_d calculated from each step to step that produced a realistic decrease in activity. Finally, the standard deviation was collected

from the average K_d calculated in Eq. 3 and the K_d calculated from the slope/intercept method in Eq. 2.

K_d values were measured vertically on each sediment layer from 2 cores collected throughout Guaymas Basin. We then selected a representative depth in the sediments (14 cm below the seafloor [cmbsf]) from which to measure K_d across all cores collected, in order to provide us with an assessment of the vertical and spatial distribution of K_d values across the study site.

2.4 Flow Rate Determination

Estimates of porewater flow rate are calculated beginning with Eq. 4 (as per Peterson, 2019):

$$Ra_t = \frac{\lambda_{Th-228}\lambda_{Ra-224}}{\lambda_{Ra-224} - \lambda_{Th-228}} \frac{Ra_{eq}}{\lambda_{Th-228}} \left(e^{-\lambda_{Th-228}t} - e^{\lambda_{Ra-224}t}\right) + Ra_i e^{-\lambda_{Ra-224}t}$$

(Eq. 4)

where Ra_{eq} is the dissolved [224]Ra activity measured from the laboratory incubation experiment for a specific sediment layer, Ra_i is the initial [224]Ra activity that would flow into that specific layer as collected from the [224]Ra activity measured at sea from an adjoining source layer either above (under downward flow conditions) or below (under upward flow conditions) the specific sediment layer, Ra_t is the porewater [224]Ra activity measured in the specific sediment layer at sea, λ_{Th-228} is the [228]Th decay constant (9.99x10⁻

[4] day^{-1}), and λ_{Ra-224} is the ^{224}Ra decay constant (1.89x10^{-1} day^{-1}). Flow in the horizontal direction was not considered in the calculation (Peterson 2019).

Excess ^{224}Ra activities determined from porewater samples collected at sea serve as values for Ra_t and Ra_i, whereas the laboratory incubation experiment results serve as values for Ra_{eq}. For any specific in-situ layer (Ra_t), two adjoining Ra_i activities exist that could serve to contribute source radium to that layer. Based on the difference in activity of Ra_t and the maximum possible activity supplied from the exisiting ^{228}Th remaining on the source sediments we measured as Ra_{eq}, we can calculate a "residence time," or an estimate of the time that it would take for the in-situ radium activity measured in each specific layer to be supported. The residence time is also considered the amount of time the porefluid remains in each layer before migrating in either vertical direction. Certain scenarios exist wherein the collected data does not support flow in either vertical direction. Specifically, if the supporting ^{224}Ra activity in a specific sediment layer contradicts the measured activity in the receiving layer at equilibrium, such that there is neither a trending decrease nor an increase in activity (i.e. $Ra_i > Ra_t > Ra_{eq}$ or $Ra_i < Ra_t < Ra_{eq}$), then a flow scenario cannot be computed with the model (Peterson, 2019).

Porewater residence times are computed for every sediment core layer under assumptions of both upward and downward flow conditions, with the exception of the very top and bottom layers of the core which only had one flow scenario computed (+z into the topmost layer from the layer below and –z into the bottommost layer from the one above). Subsequently, for each layer in which a flow condition yielded a solution, we then converted from residence time to flow rate by dividing the porewater volume in that layer (as total sediment volume multiplied by measured porosity) by the determined residence

time. An error analysis function was built in MATLAB following a bootstrapping approach, wherein the analytical uncertainties for each measured term of Eq. 4 were considered to find the full range of possible residence times for each layer and then reduced by 30% (Peterson, 2019). The analysis considered 27 different iterations to account for addition, substraction, or omittance of error associated with each observed, parent, and initial activiy measured for the specific sediment layer. Only computed residence times less than 21 days (the time ^{224}Ra takes to "grow in" to its ^{228}Th parent) are converted to a flow rate.

2.5 Water Column Sampling

Water column samples in and around suspected hydrothermal plumes were collected using a CTD rosette on AT42-05 and a follow-up cruise to Guaymas Basin in early 2019 aboard the *R/V Falkor* (FK190211). Niskin bottles collected water samples at specific depths in the water column (1m, 5m, 10m, 50m above bottom, 5m below the plume, within the plume, and 5m above the plume) based on thermal measurements from the CTD. On deck, water was collected through a sample-rinsed tube connected to a cartridge housing a MnO_2 acrylic fiber, with a vent on the end that allowed the water to flow through the cartridge at a rate of <1 L min^{-1} (Moore and Reid, 1973). The samples were subsequently measured on the RaDeCC following the procedure outlined in Section 2.1.

Targets on AT42-05 were selected to understand the relationship and distribution of radium in end-member fluid and its subsequent dissemination into the overlying water

column. Targets for sampling on FK190211 were selected based on hydrothermal activity discovered in the CTD profile and past targets from the November cruise. Radium-224 in the water samples from thermal targets were directly compared to the measured radium in ambient temperature background samples.

3. Results and Discussion

3.1 Core Profiles and Porewater Radium Activities

Sediment core profiles varied in depth, sediment coverage, temperature gradient, and composition. Core depths collected on AT42-05 ranged from 12 to 48 cmbsf, with an average depth collected of 25.6 cmbsf. Two reference cores (from Aceto Balsamico and Cathedral Hill) were collected through brown sediment away from any indications of active venting or bacterial mat presence, while the remaining 14 cores were collected from or just outside of white, yellow, and orange bacterial mats. Orange and white bacterial mats were the most common types of mat sampled, as they are often found near each other and are sometimes referred to as "fried eggs" when the white microbial mats surround an orange mat (Teske et al., 2016). While several cores produced an oily, sulfuric smell, only 2 cores contained visual traces of oil: (1) a marginal volume of oil was found in Core 3 at approximately 35 cmbsf and (2) abundant oil was found in Core 4 beginning 8 cmbsf and continued throughout the rest of the core. Large carbonate material was also recovered in Cores 2, 4, and 14.

Temperature gradients were measured for 12 out of 16 cores and were variable across the coring sites, with a minimum average temperature of 3.6 °C in a background core to a maximum average temperature of 55.6 °C near an orange microbial mat (Figure 4). The maximum recorded temperature of 89.5 °C was measured in a core collected in a Mat Mound orange bacterial mat at 40 to 45 cmbsf; however, two cores collected in the Cathedral Hill site were already approaching +80 °C temperatures in the 15 to 20 cmbsf depth range and would likely have exceeded measurements recorded within the hottest cores collected in either Mat Mound or Aceto Balsamico at a comparable depth.

The average pore fluid volume recovered from each 4 cm vertical interval was 39 ± 6 mL, with an average porosity of 0.82 ± 0.04 (Table 2). Surface layer pore fluid volume ranged from 31 mL to 58 mL, with an average volume of 43 ± 8 mL and an average porosity of 0.87 ± 0.03. Maximum pore fluid volume in the top 12 cm of the core was measured directly beneath the surface layer at 4 to 8 cmbsf and ranged in volume from 30 to 63 mL, with an average volume measured at 46 ± 9 mL. Maximum pore fluid volumes were collected from the background cores, which were generally more porous than sediments collected in microbial mats. Whole core sediment porosity for samples collected within microbial mats averaged 0.81 ± 0.02, compared to control cores with a porosity of 0.88 ± 0.00.

Porosity decreased down core in 15 out of 16 cores collected, with the exception of Core 6, a white microbial mat core from the Cathedral Hill site. In Core 6, we measured an elevated porosity of 0.82 in the bottom most layer (8 to 12 cmbsf), compared to a surface porosity of 0.79. However, we also measured an elevated porosity in a similar depth range

of 8 to 20 cmbsf for all 5 of the remaining white microbial mat cores, as well as 4 more cores collected in orange and yellow microbial mats across the basin.

Ra-224 core-top supernatant water (bottom water) activities in the background cores were consistent in value across the different sites, averaging of 0.6 ± 0.0 dpm L^{-1}. However, bottom water activities measured from the microbial mat cores were highly divergent (Table 3). Activities for all 12 cores collected directly within a microbial mat averaged 11.2 ± 9.8 dpm L^{-1}. Orange microbial mat cores had an average bottom water activity of 9.5 ± 9.1 dpm L^{-1}, yellow mat cores had an average bottom water activity of 17.6 ± 11.8 dpm L^{-1}, and white mat cores had an average bottom water activity of 10.2 ± 8.6 dpm L^{-1}. The three highest bottom water activities were measured in a yellow microbial mat in Aceto Balsamico, an orange microbial mat in Cathedral Hill, and a white microbial mat in Aceto Balsamico (Cores 1, 5, and 10, respectively; Figure 5).

Average surface layer activities also varied widely for the microbial mat cores across the three sample sites, measuring 41.9 ± 32.1 dpm L^{-1} compared to the background cores with an average surface layer activity of 0.9 ± 0.8 dpm L^{-1}. Unlike Aceto Balsamico, where we measured higher bottom water activities on average, sediment pore fluid activity and temperature were highest in Cathedral Hill, averaging 51.1 ± 35.7 dpm L^{-1} at 14.1 °C. Aceto Balsamico surface layer activity averaged 29.8 ± 10.5 dpm L^{-1} with an average temperature of 12.1 °C, while Mat Mound activity averaged 19.8 ± 0.3 dpm L^{-1} at a temperature of 11.9 °C.

Surface activities were highest in the orange mat cores, measuring 60.0 ± 46.7 dpm L^{-1}, but lowest when averaged down the whole core at 25.8 ± 14.3 dpm L^{-1}. For white microbial mats, we see a reciprocal relationship to surface and whole core activities

measured through orange microbial mats. White microbial mats were the lowest in activity of the three microbial mat types at the surface, averaging 28.9 ± 12.1 dpm L[-1] but had the highest overall average activity of 34.3 ± 12.5 dpm L[-1]. Yellow microbial mat surface activities averaged 29.6 ± 10.9 dpm L[-1], with a down core average activity of 29.6 ± 10.9 dpm L[-1]. Orange mat cores corresponded to the highest recorded temperatures, from an average 20.°7 C at the surface to an average 47.5 °C throughout the core, where neither white nor yellow mat core averages surpassed 10 °C at the surface or 20 °C down core.

As expected, every core collected within microbial mat experienced higher in-situ ^{224}Ra activity throughout the whole core than the cores collected outside of microbial mat. However, there were no general trends in bottom water and surface layer activity across the sample sites (Figure 6). The consistency in the Mat Mound site bottom water and surface activities may be attributed to reduced number of samples at the site (n = 2), in comparison to Aceto Balsamico and Cathedral Hill (n = 4 and 8, respectively). While all of the microbial mat cores are considered to be enriched compared to the bottom water and surface layer activities measured in the background core, coring site and microbial mat presence alone do not correlate with the actual degree of enrichment measured in either the bottom water or surface layers. Therefore, bottom water/surface layer activity data indicate some other in-situ source of radium must be affecting the wide range in activities measured for microbial mat cores.

Elevated temperatures corresponded to orange microbial mat presence and to the Cathedral Hill site, both of which are consistently associated with elevated temperature measurements (Teske at al., 2016). In Core 15, where we measured a maximum difference in temperature within the first 20 cm of the core (~60 °C change to the surface layer and

~80 °C to the core top, when we consider that bottom water temperature is generally equivalent to the surrounding seawater at depth), we also measured a reciprocal (and maximum) elevation in ^{224}Ra activity. Additionally, we see this reciprocal trend of decreased radium concentration gradient with increased temperature down core to a lesser extent in the other 10 out of 11 cores with associated temperature data.

3.2 Equilibration Activities

The average pore fluid volume recovered from each 4 cm vertical interval was 45 mL ± 12 mL. Surface layer pore fluid volume ranged from 21 to 65 mL, with an average volume of 44 ± 11 mL. The range in equilibrium surface activities for cores collected directly within a microbial mat started at 5.3 ± 0.4 dpm L^{-1} in a white microbial mat from Cathedral Hill to 137.3 ± 9.7 dpm L^{-1} in an orange microbial mat in Cathedral Hill. Average surface equilibrated activities for microbial mat cores was 28.8 ± 34.2 dpm L^{-1} compared to the background cores measuring 1.9 ± 0.4 dpm L^{-1}. Aceto Balsamico and Mat Mound surface equilibrated activities were consistent, at 17.5 ± 1.8 dpm L^{-1} and 19.7 ± 3.7 dpm L^{-1}, respectively. The large degree of surface activity variation arises within the Cathedral Hill samples, where the average surface activity at equilibrium measured 35.9 ± 40.3 dpm L^{-1}.

Equilibrated surface activities were highest within the orange microbial mat sediments at 54.6 ± 49.5 dpm L^{-1} (Table 4). Even without the input of Core 14, surface activities within orange mats remained the highest at 27.1 ± 15.4 dpm L^{-1}. Equilibrated surface activities within the yellow microbial mat cores were 20.7 ± 4.5 dpm L^{-1} and 14.2

± 4.8 dpm L^{-1} within the white microbial mat cores. Whole core averages were also highest within samples collected through orange microbial mats, averaging 26.6 ± 17.5 dpm L^{-1}. However, down the core we see a reversal from surface activity trends between white microbial mat averages and yellow microbial mat averages (20.1 ± 9.1 dpm L^{-1} vs 12.3 ± 3.6 dpm L^{-1}, respectively).

For equilibration sediments, pore fluid volumes were dependent upon the mass of sediment recovered following initial centrifugation as well as the recreation of in-situ conditions in the lab. Average volumes recovered throughout the cores and in the surface layers during the equilibration experiments were higher on average but still aligned closely with the volumes recovered at-sea. Conditions for processing sediments in a lab are much more favorable to those at-sea, where the risk for sample loss is increased from the initial sample collection until it is brought on board and processed. Additionally, we recreated in-situ conditions based on bulk density and porosity calculations simulating an ideal environment; therefore, some discrepancy between recovered pore fluid in the lab and at-sea was expected.

Unexpectedly, whole core ^{224}Ra in-situ activities for 10 out of 16 cores were higher than their equilibrium activities. Due to the nature of isotopic in-growth and decay, we expect to see maximum ^{224}Ra activity at equilibrium, sourced from its thorium parent. The background core activities illustrate this relationship, where whole core equilibrium activities are ~10 dpm L^{-1} higher than those measured at-sea. Therefore, there must be some source mechanism happening to force the disequilibrium in this direction, where in-situ activities are higher than those we see from the incubation experiments within the majority

of the microbial mat cores. The implication of disequilibrium results are explored further in section 3.4.

3.3 Radium-224 Partitioning

Sediment masses (M_s) for each sample processed for the radium partitioning experiment ranged from ~15 to 45 g, and averaged 29 ± 7 g across the 12 to 16 cmbsf depth range for all 16 cores. The volume of radium-free seawater added to the samples (V_T) ranged from ~100 to 200 mL, with an average volume added of 162 ± 37 mL. Aliquot volumes (ΔV) ranged from 18 to 52 mL, with an average aliquot volume across the 16 cores of 35 ± 9 mL.

Ra-224 activities measured directly on the RaDeCC (λC_i in Eq.2) following the completion of the radium partitioning experiments ranged from a starting activity of 0.2 ± 0.0 dpm L^{-1} to 25.9 ± 1.7 dpm L^{-1}. For cores where depleting activities of ^{224}Ra were consistent after each removal step, final activities (λC_{i-1}) after the fourth removal step ranged from 0.9 ± 0.1 dpm L^{-1} to 10.1 ± 0.6 dpm L^{-1}. Uncertainties in activity are determined by the total counts logged on the RaDeCC over time, taking into consideration natural isotopic decay. Unlike the in-situ or equilibrium ^{224}Ra activities measured in 3.1 and 3.2, λCi activities are only the amount of radium moved into solution over the 24 hour course of the incubation period and represent the starting point for the calculation.

The first core processed in its entirety (Core 9) ranged in initial activity from 1.8 ± 0.2 dpm L^{-1} to 25.9 ± 1.7 dpm L^{-1}. Seven, 4 cm layer depths were processed; of these 7 samples, 5 samples resulted in likely K_d values (where either Eq. 2 or 3 was applicable).

We report the average K_d through the core as 3.9 ± 2.3 dpm L^{-1}. The second whole core processed (Core 15) ranged in initial activity from 0.2 ± 0.0 dpm L^{-1} to 43.8 ± 2.8 dpm L^{-1}. Eight, 4 cm layer depths were processed, and 6 samples resulted in likely K_d values. We calculated the average K_d through Core 15 as 2.1 ± 0.9 dpm L^{-1}.

Following Eq. 2 and 3, K_d values across layer 4 (12 to 16 cmbsf) of all 16 cores averaged 2.5 ± 0.6 L kg^{-1} (Table 5). The highest partitioning value of 6.5 ± 2.5 L kg^{-1} occurred at the Cathedral Hill coring site (Core 14); however, on average, the Aceto Balsamico cores had higher K_d values at 2.9 ± 0.5 L kg^{-1}, than at Cathedral Hill where an average K_d value of 2.5 ± 0.7 L kg^{-1} was found, and at Mat Mound where an average of 1.7 ± 0.06 L kg^{-1} was observed. Interestingly, the lowest K_d value was also reported in the Cathedral Hill venting site at 0.8 ± 0.1 L kg^{-1} (Core 6), within a white microbial mat.

Partitioning values calculated for orange microbial mat cores averaged 2.9 ± 2.2 dpm L^{-1}, with a range of 0.94 ± 1.09 dpm L^{-1} measured in a Cathedral Hill core (Core 5) to the value measured in Core 14. Yellow microbial mat Kd values averaged 2.6 ± 0.9 dpm L^{-1} with a range in values of 1.7 ± 0.7 dpm L^{-1} to 3.6 ± 0.6 dpm L^{-1}. White microbial mat K_d values averaged 2.4 ± 1.2 dpm L^{-1}, from the minimum value measured in Core 6 to a maximum value of 4.5 ± 1.1 dpm L^{-1}. Background cores also averaged 2.4 ± 0.8 dpm L^{-1}, with a minimum value of 1.7 ± 0.5 dpm L^{-1} to a maximum value of 3.2 ± 1.6 dpm L^{-1}.

Nine of the sediment cores followed the anticipated trend of depleted activities over the course of the experiment and were plotted according to the Colbert and Hammond (2009) equation (Eq. 2; Figure 8). In the remaining samples processed for K_d, 1 or more steps did not result in a depleted activity from the preceding sample activity measured. When deciding initially which layer to use in order to calculate a representative K_d value

across the basin, we considered our whole core experimental results as well as experimental data from Peterson (2019), who found consistent partitioning in the 4 to 20 cmbsf depth range. K_d calculated in layer 4 for Core 9 (12 to 16 cmbsf) was associated with the least amount of error (for all layers in Cores 9 and 15) at 3.4 ± 0.4 dpm L^{-1} and was the only layer in Cores 9 and 15 that behaved according to expected isotopic behavior following the Colbert and Hammond (2008) procedure and results.

Experimental error clearly affected the results of the initial experiments on Cores 9 and 15. We considered that the method of aggravating the slurry during the 24 hour incubation period was likely too aggressive. For the remaining 14 cores, slurry bottles were gently mixed during the incubation period. Additionally, during the removal process between the aliquot removal and addition step, the volume of Ra-free seawater added to the slurry bottle was added in such a way to minimize disturbance to the sediment, as it was believed that enriched pore fluid in the original experiments were likely sampled during the entirety of the experiment as sediments were continually disturbed, artificially inflating the activity of ^{224}Ra being released into solution by its ^{228}Th parent. Results for the remaining 14 cores were associated with greatly reduced error in comparison and λC_{i-1} activities were far more consistent.

An ANOVA test was conducted to understand the spatial significance of K_d across the basin (i.e. were there any significant relationships among K_d values for cores collected in Mat Mound vs Cathedral Hill or Aceto Balsamico?), as well as the K_d association with mat presence/composition (Table 6). Although the trend in highest K_d values to lowest K_d values appeared to correlate with in-situ microbial mat composition activities, our results show a relatively small effect size/$\eta^2 = 0.04$; only ~4% of the variation in K_d is explained

by sample site or mat presence/composition. We also considered thermal profiles through the cores. A plot of K_d and temperature for the 12 out of 16 cores with accompanying thermal profile data indicates no relationship between K_d and sediment temperature (R^2 = 0.00; Figure 7). Our findings indicate K_d neither differs significantly across the basin nor does it appear to have a relationship with sediment temperature, mat presence or composition.

Peterson (2019) measured K_d on one core (Core 10) from the AT 42-05 cruise and reported a 15.6 ± 1.8 L kg^{-1} value. In the same core, we report a K_d value of 2.1 ± 0.3 L kg^{-1}. The Peterson (2019) value was measured from the bottom layer of the core (28-32 cm depth), whereas we report K_d values from the upper-mid core depth (12-16 cm), yet the reported values remain relatively comparable, agreeing within an order of magnitude.

3.4 Effective Fluid Flux

3.4.1 Residence Time

In order to compute effective fluid flux through the sediments, residence time must first be calculated. The Peterson (2019) model accounts for the change in in-situ ^{224}Ra activity vertically (*Ra$_i$* and *Ra$_t$*), between each layer in both the upward (out of the sediments) and downward (into the sediments) flow direction, considering the potential to be supported—calculated from the equilibration activities (*Ra$_{eq}$*).

Based on the activities measured in the background core collected in Aceto Balsamico, no solution was possible in the upward transport direction. A solution imposing a downward transport direction for Core 12 resulted in an average pore fluid residence time

of 0.18 ± 0.05 days. The Cathedral Hill background core activities also failed to support a solution under upward flow conditions. An average residence time of 0.68 ± 0.49 days was calculated in Core 16 in the downward transport direction. When averaged together, background residence times are 0.43 ± 0.25 days.

In the surface layer, orange microbial mat cores range from no solution (residence time <0.1 days) to 9.68 ± 4.88 days (Core 14), with an average residence time of 3.77 ± 4.19 days. Estimates at the surface layer can only be considered in the upward vertical transport direction, given only 1 value for Ra_i exists to support the surface layer activity (Ra_t). Average residence time for vertical transport in the upward direction for orange microbial mat cores was 1.97 ± 1.89 days and 3.34 ± 2.95 days in the downward direction. Only layers that yielded a residence time are included in core averages.

Pore fluid residence time in the surface layers of the 2 yellow microbial mat cores ranged from no solution (residence time <0.1 days, Core 4) to 2.36 ± 1.34 days (Core 1). In Core 1, an average upward residence time through the whole core was 1.26 ± 0.68 days and 0.42 ± 0.32 days in the downward direction. Core 4 yielded an average downward residence time of 2.58 ± 2.68 days and no solution in the upward transport direction.

Surface layer residence time of pore fluid through the white microbial cores ranged from no solution (residence time <0.1 days) to 1.11 ± 0.28 days (Core 7), with an average surface residence time of 0.84 ± 0.27 days. Two of the cores collected through white microbial mats did not yield an upward transport solution at any depth (Cores 6 and 13). Average residence time through the whole core in the upward transport direction for the remaining 4 cores was 4.75 ± 3.30 days. Only 1 white microbial mat core did not yield a

down core solution (Core 9). The average core residence time in the downward direction for the remaining cores was 1.75 ± 0.30 days.

Porewater residence time down the cores decreased dramatically with depth (Figure 9) and is likely a result of the decreased porosity of the sediments, as decreased pore space would reduce contact time in a scenario of constant, vertical velocity (Peterson, 2019). Flow in the downward direction yielded a potential solution for every core, whereas flow in the upward direction only yielded a potential solution for 12 out of 16 cores. Flow in the downward direction yielded a likely solution for the top 16 cm of the core for 7 out of 16 cores and the bottommost layers of the core for 8 out of 16 cores. For the seven cores that showed potential downward flux occurring in the bottommost layers, an upward direction for the topmost layers of the core also yielded a solution. For each layer that met the flow conditions of the model, flow rates were calculated as described in the methods.

3.4.2 Flow Rate

Discharge (upward fluid flux) estimates, across Guaymas Basin tended to be more regular, ranging from 1.21 ± 0.84 mL cm^{-2} d^{-1} to 5.76 ± 0.76 mL cm^{-2} d^{-1} compared to recharge (downward fluid flux) rates, ranging from 1.63 ± 0.16 mL cm^{-2} d^{-1} to 20.07 ± 5.21 mL cm^{-2} d^{-1}. Flux results in the upward direction were also typically more conservative than those reported in the downward direction at 2.9 ± 0.3 mL cm^{-2} d^{-1} vs 6.5 ± 1.7 mL cm^{-2} d^{-1} (Table 7; Figure 10).

Fluid flux rates through the mat cores, in either flux direction, were fairly consistent (Figure 11). Effective fluid flux through orange microbial mat cores were predominately in the recharge direction within the top 16 cm of the sediment core, ranging from 1.2 ± 0.8

27

mL cm^{-2} d^{-1} in Core 14 to 5.8 ± 1.8 mL cm^{-2} d^{-1} in Core 2, at an average rate of 3.1 ± 1.9 mL cm^{-2} d^{-1}. One orange mat core (Core 5) showed some evidence of recharge at 14 cmbsf, at a rate of 3.1 ± 1.4 mL cm^{-2} d^{-1}; however, the top three vertical layers only yielded a solution in the downward flow direction at an average rate of 1.7 ± 0.9 mL cm^{-2} d^{-1}.

Yellow microbial mat cores experienced similar effective fluid flux rates to each other but in the opposite vertical direction. For Core 1, from the Aceto Balsamico yellow microbial mat, we calculated a discharge effective flux rate of 3.4 ± 1.34 mL cm^{-2} d^{-1}. In the Cathedral Hill yellow microbial mat (Core 4), we calculated a recharge flow rate of 3.9 ± 1.0 mL cm^{-2} d^{-1}. White mat cores predominately experienced pore fluid recharge into the sediments, at an average rate of 2.7 ± 1.2 mL cm^{-2} d^{-1}. For the 2 white mat cores with a discharge solution, we calculated an average flux rate of 2.3 ± 0.0 mL cm^{-2} d^{-1}.

Peterson (2019) reported that flow can change direction and magnitude through the length of a sediment core, with results averaging 3.6 ± 0.6 mL cm^{-2} d^{-1} for mat-covered cores collected in Guaymas Basin in 2016 (cruise AT37-06). Our results show an average effective fluid flux of 2.8 ± 1.3 mL cm^{-2} d^{-1} for mat-covered cores collected in Guaymas Basin on AT42-05 in either flow direction. For the cold seep environments of the Gulf of Mexico, Peterson (2019) describes downward fluid fluxes using the same methods as those in Guaymas Basin for several seep cores where downward transport was unexpected. However, the same study only observed 1 out of 19 cores collected on AT37-06 in Guaymas Basin with a negative fluid flux (a large discrepancy between both data sets where half off AT42-05 cores showed negative flux; Table 8), and suggested the high volume of positive flux was due to coring bias in the elevated, temperature-driven mat sediments.

Positive, or upward, flux showed weak positive correlation with temperature (the maximum reported average temperature of 61 °C corresponded with the greatest effective fluid flux in the upward direction) while negative flux showed a negative correlation with average core temperature (Figures 12). The background cores, collected in low temperature sediments, show downward fluid flux. We expect low temperature cores to correlate with downward flux preferentially over high temperature cores (although low temperature cores may still experience upward vertical transport) and suspect that stronger correlation results concerning upward flow at hotter temperatures would follow with more temperature and flux data.

Episodic variation in high to low temperature dynamics across Guaymas Basin could result in data that may not correlate with expected results, such as several mat cores collected on AT42-05 that are associated with low temperature measurements (McKay et al., 2012; Meyer, 2013). High temperature fluid flux may have been present shortly before measurements were collected, actually driving the specific biogeochemical profile sampled during an episode of cooler fluid flow. The erratic variation in temperature regimes may also explain why the hottest core measured on AT42-05 (Core 15, ID: CH41) in the upper 16 cm resided just outside of an orange mat, where horizontal migration of the hydrothermal fluid flux could have recently occurred. The unexpected temperature profile of Core 15 may also explain the inconsistent fluid flux happening within the core, given that the half-life of ^{224}Ra is 3.66 days and that episodic variation of the flow can occur on a daily timeframe. A lingering radium signature, if captured within the time frame between post-fluid migration and pre-decay (without considering any input from thorium on the sediments), could likely produce skewed flux data.

While we expected to see consistent hydrothermal discharge occurring in the upward vertical direction across Guaymas Basin, especially through bacterial mat sediments, our data show an equal number of cores experiencing downward fluid flux. However, the unpredictable pattern of fluid flux, differing so greatly from results reported by Peterson (2019), is not improbable. The area likely experiences rapid and chaotic changes in temperature and fluid flux regimes, often on a daily scale, driven in part by the erratic hydrothermal fluid supply and surficial mixing of cold bottom water exchanging with the sediments (Gundersen et al., 1992; Meyer, 2013). Given that hydrothermal recharge mechanisms and locations are notoriously difficult to identify and characterize (Johnson et al., 2010), the vertical exchange model used in this study could provide further insight on this relatively invisible and highly irregular type of fluid flux.

Finally, we calculated no correlation between the measured effective fluid flux rates and the calculated radium partitioning values from Section 3.3 ($R^2 = 0.00$; Figure 13). Considering that reported K_d values from the literature range from 0 to 5,000 L kg^{-1} in seawater (Beck and Cochran, 2013), the close alignment with the Peterson (2019) findings to our own measurements supports our hypothesis that the radium partitioning across the basin is relatively homogenous, and, therefore, is not necessary to consider when calculating effective fluid flux rates, via ^{224}Ra isotopes, through Guaymas Basin sediments.

3.5 Radium-224 Water Column Signatures

Twenty-one casts within Guaymas Basin were sampled for radium (AT42-05 and FK190211; Appendix I), and one cast was sampled in the Pescadero Basin (FK190211), a

known vent field approximately 400 km farther south. Bottom temperatures outside of the hydrothermal plume ranged from 2.6 °C at the control site to 2.9 °C when approaching areas of active venting and up to ~6 °C in two separate casts. A thermal spike within the bottom 100 m of the water column over 2.9 °C was considered to be in or near an area of active hydrothermal fluid flow. Two control casts were sampled in order to develop a baseline for ^{224}Ra enrichment in the surrounding seawater.

3.5.1 Guaymas Basin

Water volumes sampled on AT42-05 ranged from ~10 to 45 L, with an average volume sampled of 29 ± 9 L. On FK190211, water volumes sampled ranged from ~10 to 30 L, with an average volume sampled of 18 ± 6 L. In addition to the sites sampled for sediment cores, 1 other site was sampled on AT42-05 for radium within the water column (Big Pagoda). Six additional sites were also sampled on FK190211. In total, 10 unique sites within Guaymas Basin (not including the control casts) were sampled for water column radium enrichments.

The two control casts sampled were in separate sites and both casts maintained an ambient water column temperature at depth of 2.6 °C (Appendix I). Depths sampled within the control cast on AT42-05 ranged from 1690 to 2001 m, while the maximum depth of the control cast on FK190211 was nearly 500 m shallower, at a range of 1483 to 1583 m. On AT4205, background ^{224}Ra activities ranged from 0 to 1.7 dpm 100L^{-1}, with an average activity of 0.8 ± 0.6 dpm 100L^{-1}. In comparison, control water did not contain a resolvable ^{224}Ra activity in the water column on FK190211, with the exception of the bottommost

depth sampled, where an activity of 1.4 ± 0.0 dpm 100L^{-1} was detected. Average ^{224}Ra activity for the entire FK190211 control cast was 0.4 ± 0.0 dmp 100L^{-1}.

Water column activities at depth on AT42-05 ranged from 0.8 ± 0.6 dpm 100L^{-1} over the Big Pagoda vent site to 44.3 ± 2.7 dpm 100L^{-1} within the Cathedral Hill vent site. Within the bottom ~150 m of a cast, ^{224}Ra activities on AT42-05 averaged 7.1 ± 11.2 dpm 100L^{-1} (activity averages exclude control casts but do include casts not sampled within a thermal spike). Water column activities at depth on FK190211 ranged from undetectable levels in the Big Cactus vent site to 36.3 ± 2.6 dpm 100L^{-1} within the Big Pagoda vent site. Within the bottom ~150 m of a cast, ^{224}Ra activities on FK190211 averaged 6.5 ± 20.0 dpm 100L^{-1}.

All 3 Big Pagoda casts where niskins were successfully fired within the thermal anomaly were 1 to 2 orders of magnitude higher than activities measured in the control casts. The second highest ^{224}Ra activity measured on AT42-05 was 39.2 ± 2.2 dpm 100L^{-1} before dropping to 17.0 ± 1.6 dpm 100L^{-1}, in the 'Big Pagoda 2' cast, captured within a thermal spike of 3.30 °C. Similarly, on FK190211, the highest measured ^{224}Ra activities were both collected from the 'Big Pagoda 2 and 3' casts at 34.3 ± 2.4 dpm 100L^{-1} in water measuring 3.3 to 4.5 °C and 37.1 ± 2.6 dpm 100L^{-1} in water measuring 3.9 to 5.4 °C, respectively. In total, 10 out of 14 casts capturing hydrothermal plumes on AT42-05 and FK190211 (where a thermal spike was registered), a corresponding radium signature was also measured (Figures 14 & 15).

The first Big Pagoda cast collected on FK190211 was only sampled at the bottommost depth of 2006 m and showed a slight radium enrichment of 1.7 ± 0.1 dpm 100L^{-1}, although we do not believe a direct hydrothermal sample was captured given that

the recorded temperature at the time of sampling was only 2.9 °C. Samples within the 2.9 to 3.1 °C temperature range in Guaymas Basin often showed a weak radium signal, at approximately 1.0 to 3.0 dpm 100L-[1], compared to the control site, which only showed a weak signal at the bottommost depth (1903 m), and could be attributed to slow seepage through the sediments. The control cast on AT42-05 showed a weak radium enrichment in 4 out of 5 depths sampled; however, the site of the control cast was within the Cathedral Hill venting area and may have captured some signature of a dispersed plume.

The most compelling evidence for the usage of ^{224}Ra as a tool for tracking hydrothermal plumes comes from the fact that, in many cases, we were still able to detect a small radium enrichment in samples that were not collected inside of the thermal signature on the CTD, in the area where we assume the plume has achieved neutral buoyancy and is starting to disperse (compared to the background levels in the control casts; Table 9). The 6 other casts sampled in Guaymas Basin on FK190211 were over known areas of venting, and although the CTD rosette was unable to capture the plume, we still see a relative radium enrichment within the water column in 4 out of 6 casts.

Changes in the physical characteristics of suspected hydrothermal plumes, such as temperature, conductivity, and turbidity are necessary and valuable tools for finding hydrothermal vents and can be tracked by a ship's CTD sensor. Additionally, the chemical characteristics of the plume can also be tracked through the use of certain trace metals like P, Fe, and Cu, which, unlike the CTD, can also track the neutrally buoyant plume water hundreds of meters away from the source (Feely et al., 1992). Employing ^{224}Ra can potentially serve as another tool for this process, especially due to the quick nature of the sampling and supplemental results. The benefit of using radium as a tracer means that water

33

column samples are collected onboard and are directly analyzed on the RaDeCC. Field measurements are processed immediately, without the delay of returning to a permanent lab, and thorium corrections have only a minor effect on water column samples. We feel there is a strong potential to track a hydrothermal plume in real-time via ^{224}Ra isotopes, but additional sampling would increase our confidence in this assessment.

3.5.2 Pescadero Basin

The Pescadero cast successfully sampled within a particularly strong thermal signature. Three niskins at approximately 4 km deep were sampled for ^{224}Ra. Enriched radium activity in the hydrothermal plume was an order of magnitude higher than the highest recorded activity in Guaymas Basin, measuring 137 ± 9.5 dpm 100L^{-1} at a bottom depth of 3.7 km and a thermal spike of 5.6 °C (Figure 16). Although no associated control casts were collected in the Pescadero Basin, background levels of radium activity should be relatively similar to those found further north in the Guaymas Basin. When the third niskin sampled fired outside of the thermal spike at 1.9 °C, no resolvable ^{224}Ra activity was detected. Given that the measured activity was enriched, even when compared to the maximum activity measured in Guaymas Basin, we can safely assume that the radium signatures we recorded for Pescadero Basin are a reliable indicator of active hydrothermal fluid flow before visual or bathymetric confirmation.

Bottom depths in the Pescadero Basin range around 4 km deep and are nearly 2 km deeper than the maximum depths in Guaymas Basin. Prior to 2012, the more southern Pescadero Basin was thought to be hydrothermally inactive (Paduan et al., 2018). However, dedicated mapping expeditions in 2015 confirmed 6 actively discharging chimneys. Like

Guaymas Basin, the Pescadero site has a thick sediment package overlying the basin floor with a similar sediment and hydrothermal fluid geochemistry, although the discharging flow was noted to be "clear," rather than the more typical black smokers (Paduan et al., 2018). The suspected vent identified on FK190211 can be cross-checked by the Paduan et al. (2018) study, as their AUV mapping discovered a particularly large active vent at the same GPS location as our sample cast in Pescadero Basin (denoted as 'Z' seen in Figure 17).

4. Conclusions

Sixteen sediment cores collected in Guaymas Basin were evaluated to understand the potential relationships between radium partitioning, effective fluid flux through the sediments, thermal profiles, and microbial mat presence and composition. These results were then compared to previous work, using the same vertical exchange model developed in Peterson (2019), to assess the assumption that K_d in Guaymas Basin is homogenous across the seafloor and plays no role in the other geochemical and physical anomalies observed in the basin. Finally, water column samples were collected on two cruises to Guaymas Basin to test the functionality of using ^{224}Ra isotopes to identify and track hydrothermal plumes once those plumes have achieved neutral buoyancy and dispersed.

K_d values showed no correlation with effective fluid flux measurements ($R^2 = 0.00$), and functionally no correlation with temperature, mat presence/composition, or distance across the basin ($R^2 = 0.04$). Given the large magnitude range for potential K_d values in seawater (Beck and Cochran, 2013), the reported range in K_d values from this study (0.84

$\pm$ 0.11 L kg^{-1} to 6.48 $\pm$ 2.48 L kg^{-1}) supports our hypothesis that radium partitioning across Guaymas Basin is homogenous and independent of external influences such as thermal gradient, effective fluid flux, or microbial mat presence.

Effective fluid flux results were unexpected, as we predicted that our results would align with the results from Peterson (2019), whose results showed stronger upward fluid flux across the sediments whereas we noted fluid transport in the downward direction in at least half of the cores collected. However, these results are not unlikely given the well-documented, rapid and chaotic changes in temperature and fluid flux regimes across Guaymas Basin (Gundersen et al., 1992; Meyer, 2013).

Employing cross analysis between the Paduan et al. (2018) study, the CTD profile of the FK190211 cast, and the corresponding enrichment of ^{224}Ra supports our hypothesis that radium is a reliable tool for measuring hydrothermal fluid flow, and our ability to detect a radium signal after a thermal signature is no longer present indicates that radium can be a potentially valuable tool for tracking hydrothermal plumes further into the water column. Additional sample collection/analysis is certainly warranted to better understand the potential of utilizing ^{224}Ra as tracer of dispersed, ambient plume water into the surrounding ocean.

References

Alt, J., 1995. Subseafloor Processes in Mid - Ocean Ridge Hydrothermal Systems.
    Geophysical Monograph 91, American Geophysical Union, 85-114.
    doi.org/10.1029/GM091p0085

Ballard, R.D., 1977. Notes on a major oceanographic find. Oceanus vol. 20.3., Woods
    Hole Oceanographic Institution

Beck, A.J., Cochran, M.A., 2013. Controls on solid-solution partitioning of radium in
    saturated marine sands. Marine Chemistry, Radium and Radon Tracers in Aquatic
    Systems 156, 38–48. doi.org/10.1016/j.marchem.2013.01.008

Berner, R.A., 1980. Early diagenesis-a theoretical approach. Princeton Series in
Geochemistry,
    Princeton University Press.

Bris, N.L., Arnaud-Haond, S., Beaulieu, S., Cordes, E., Hilario, A., Rogers, A., van de
Gaever,
    S., Wantanabe, H., 2016. Chapter 45. Hydrothermal vents and cold seeps. The
First
    Global Integrated Marine Assessment – World Oceans Assessment.

Buckley, A., B.J. MacGregor, and A. Teske. 2019. Identification, expression and activity
    of candidate nitrite reductases from orange *Beggiatoaceae*, Guaymas Basin.
    Frontiers in Microbiology 10:644, doi:10.3389/fmicb.2019.00644.

Burnett, B., Chanton, J., Christoff, J., Kontar, E., Krupa, S., Lambert, M., Moore, W.,
    O'Rourke, D., Paulsen, R., Smith, C., Smith, L., Taniguchi, M., 2002. Assessing
    methodologies for measuring groundwater discharge to the ocean. *Eos,
    Transactions American Geophysical Union*, *83*(11), 117–123.
    doi.org/10.1029/2002EO000069

Campbell, A. C., and Gieskes, J.M., 1984. Water column anomalies associated with
    hydrothermal activity in the Guaymas Basin, Gulf of California, Earth Planet. Sci.
    Lett., 68, 57-72

Campbell, A. C., et al., 1988. Chemistry of hot springs on the Mid- Atlantic Ridge,
    Nature, 335, 514-519

Campbell, A. C., C. R. German, M. R. Palmer, T. Gamo, and J. M. Edmond., 1994
    Chemistry of hydrothermal fluids from the Escanaba Trough, Gorda Ridge, in
    Geologic, Hydrothermal and Biological Studies of Escanaba Trough, Gorda
    Ridge, Offshore Northern California, edited by J. L. Morton, R. A. Zierenberg,
    and C. A. Reiss, U.S. Geol. Surv. Bull., 2022, 201-221.

Calvert, S.E., 1966. Accumulation of diatomaceous silica in the sediments of the Gulf of California, Geological Society of America. Bull., v. 77, 569-596.

Charette, M., K. Buesseler, and J. Andrews. 2001. "Utility of Radium Isotopes for Evaluating the Input and Transport of Groundwater-Derived Nitrogen to a Cape Cod Estuary." *Limnology and Oceanography*. 46(2): 465-470. doi.org/10.4319/lo.2001.46.2.0465

Childress, J. J. and Fisher, C. R. 1992. The biology of hydrothermal vent animals: physiology, biochemistry, and autotrophic symbioses, Oceanogr. Mar. Biol. Annu. Rev., 30, 337–441

Colbert, S.L., Hammond, D.E., 2008. Shoreline and seafloor fluxes of water and short-lived Ra isotopes to surface water of San Pedro Bay, CA. Marine Chemistry 108, 1–17. https://doi.org/10.1016/j.marchem.2007.09.004

Corliss, J.B., and Ballard, R.D., 1977. Oases of life in the cold abyss. National Geographic Magazine, 152: 441-453.

Einsele, G., Gieskes, J. M., Curray, J., Moore, D. M., Aguayo, E., Aubry, M.-P.,Vacquier, V. 1980. Intrusion of basaltic sills into highly porous sediments, and resulting hydrothermal activity. *Nature*, *283*(5746), 441–445. doi.org/10.1038/283441a0

Feely, R. A., Massoth, G. J., Baker, E. T., Lebon, G. T., and Geiselman, T. L. 1992. Tracking the dispersal of hydrothermal plumes from the Juan de Fuca Ridge using suspended matter compositions, *J. Geophys. Res.*, 97(B3), 3457– 3468, doi:10.1029/91JB03062.

German, C.R., and K.L. Von Damm. 2003. Hydrothermal processes. Pp. 181–222 in Treatise On Geochemistry, Volume 6: The Oceans and Marine Geochemistry. H.D. Holland and K.K. Turekian, eds, Elsevier, London.

Gieskes, J.M., Kastner, M., Einsele, G., Kelts, K., and Niemitz, J., 1982. Hydrothermal activity in the Guaymas Basin, Gulf of California: a synthesis. In Curray, J.R., Moore, D.G., et al., *Initial Reports of the Deep Sea Drilling Project*, 64: Washington, DC (U.S. Government Printing Office), 1159–1167. doi.org/10.2973/dsdp.proc.64.155.1982

Grassle J.F., 1983. Introduction to the Biology of Hydrothermal Vents. In: Rona P.A., Boström K., Laubier L., Smith K.L. (eds) Hydrothermal Processes at Seafloor Spreading Centers. NATO Conference Series (IV Marine Sciences), vol 12. Springer, Boston, MA

Gundersen, J.K., Jorgensen, B.B., Larsen, E., Jannasch, H.W., 1992. Mats of giant
sulphur bacteria on deep-sea sediments due to fluctuating hydrothermal flow.
Nature 360, 454. doi.org/10.1038/360454a0

Jannasch, H. W., 1983. Microbial processes at deep sea hydrothermal vents, in
Hydrothermal Processes at Seafloor Spreading Centers, edited by P. A. Rona, K.
Bostr6m, L. Laubier, and K. Smith, pp. 677-709, Plenum, New York

Jannasch, H. W., 1995. Microbial interactions with hydrothermal fluids in Seafloor
Hydrothermal Systems: Physical, Chemical, Biological, and Geological
Interactions, Geophys. Monogr. Ser., vol. 91, edited by S. E. Humphris, R. A.
Zierenberg, L. S. Mullineaux, and R. E. Thomson, pp. 273-296, AGU,
Washington, D.C.

Johnson, H.P., Tivey, M.A., Bkorkland, T.A., and Salmi, M.S. 2010. Hydrothermal
circulation within the Endeavor Segment, Juan de Fuca Ridge. Geochemistry
Geophysics Geosystems 11,Q05002. doi.org/10.1029/2009GC002957

Kadko, David. 1996. Radioisotopic Studies of Submarine Hydrothermal Vents. Reviews
of Geophysics 34.3: 349-66. doi.org/10.1029/96RG01762

Kastner M. 1982. "Evidence for two distinct hydrothermal systems in the Guaymas
Basin," in *Initial Reports of the Deep Sea Drilling Project*, eds Curray J. R.,
Blakeslee J., Platt L. W., Stout L. N., Moore D. G., Aguayo J. E. (Washington,
DC: U.S. Government Printing Office;), 1143–1158.

Krest, J., W.S. Moore, L. R. Gardner, and James Morris., 2000. "Marsh Nutrient Export
Supplied by Groundwater Discharge: Evidence from Radium Measurements."
doi.org/10.1029/1999GB001197

Krest, J.M., Harvey, J.W., 2003. Using natural distributions of short-lived radium
isotopes to quantify groundwater discharge and recharge. Limnology and
Oceanography 48, 290–298. doi.org/10.4319/lo.2003.48.1.0290

Krishnaswami, S., Graustein, W. C., Turekian, K. K., and Dowd, J. F., 1982. Radium,
thorium and radioactive lead isotopes in groundwaters: Application to the in situ
determination of adsorption-desorption rate constants and retardation
factors, *Water Resour. Res.*, 18(6), 1663– 1675, doi: 10.1029/WR018i006p01663.

Lambe, T.W., 1951. Soil testing for engineers. Series in Soil Engineering, Wiley.

Lapham, L., Alperin, M., Chanton, J., Martens, C., 2008. Upward advection rates and
methane fluxes, oxidation, and sources at two Gulf of Mexico brine seeps. Marine
Chemistry 112.

Levin, L. A., Baco, A. R., Bowden, D. A., Colaco, A., Cordes, E. E., Cunha, M. R., … Watling, L. 2016. Hydrothermal Vents and Methane Seeps: Rethinking the Sphere of Influence. *Frontiers in Marine Science*, *3*, 72. doi.org/10.3389/fmars.2016.00072

Little, C.T.S., Vrijenhoek, R.C., 2003. Are hydrothermal vent animals living fossils? Trends in Ecology & Evolution 18, 582–588. doi.org/10.1016/j.tree.2003.08.009

Lizarralde, D., Axen, G.J., Brown, H.E., Fletcher, J.M., González-Fernández, A., Harding, A.J., Holbrook, W.S.,et al., 2007. Variation in styles of rifting in the Gulf of California. *Nature*, 448(7152):466–469. doi.org/10.1038/nature06035

Lonsdale, P., 1978. Submersible exploration of Guaymas Basin. SIORef. 78-1 (Reports, Scripps Institution of Oceanography).

Lonsdale, P. F., Bischoff, J. L., Burns, V. M., Kastner, M., and Sweeney, R. E., 1980. A high-temperature hydrothermal deposition the sea bed at a Gulf of California spreading center. *Earth Planet*. Sci. Lett., 49:8-20

McKay, L.J., B.J. MacGregor, J.F. Biddle, H.P. Mendlovitz, D. Hoer, J.S. Lipp, K.G. Lloyd, and A.P. Teske. 2012. Spatial heterogeneity and underlying geochemistry of phylogenetically diverse orange and white *Beggiatoa* mats in Guaymas Basin hydrothermal sediments. Deep-Sea Research I, 67:21-31.

McKay, L., Klokman, V.W., Mendlovitz, H.P., LaRowe, D.E., Hoer, D.R., Albert, D., Amend, J.P., Teske, A., 2016. Thermal and geochemical influences on microbial biogeography in the hydrothermal sediments of Guaymas Basin, Gulf of California. Environmental Microbiology Reports 8, 150–161. doi.org/10.1111/1758-2229.12365

Meyer, S., Wegener, G., Lloyd, K., Teske, A., Boetius, A., & Ramette, A. 2013. Microbial habitat connectivity across spatial scales and hydrothermal temperature gradients at Guaymas Basin. *Frontiers in Microbiology*, *4*, 207. doi.org/10.3389/fmicb.2013.00207

Moore, W. S., and Reid, D. F. 1973. Extraction of radium from natural waters using manganese-impregnated acrylic fibers, *J. Geophys. Res.*, 78(36), 8880– 8886, doi:10.1029/JC078i036p08880.

Moore, W.S., 1976. Sampling ^{228}Ra in the deep ocean. Deep-Sea Research 23, 647-651.

Moore W.S., and Arnold R., 1996. Measurement of ^{223}Ra and ^{224}Ra in coastal waters using a delayed coincidence counter. Journal of Geophysical Research: Oceans 101, 1321–1329. doi.org/10.1029/95JC03139

Moore, W.S., 2000. Ages of continental shelf waters determined from ^{223}Ra and ^{224}Ra. Journal of
Geophysical Research. 105:C9, 22117-22122.

Moore, W.S., 2008. Fifteen years' experience in measuring ^{224}Ra and ^{223}Ra by delayed-coincidence counting. Marine Chemistry, Measurement of Radium and Actinium Isotopes in the marine environment 109, 188–197. doi.org/10.1016/j.marchem.2007.06.015

Nelson, D.C. and Jannasch, H.W., 1983. Chemoautotrophic growth of a marine Beggiatoa in sulfide-gradient cultures. Arch Microbiol 136:262–269

Nelson, D.C., Wirsen, C.O., Jannasch, H.W., 1989. Characterization of large, autotrophic *Beggiatoa* spp. abundant at hydrothermal vents of the Guaymas Basin. Applied and
Environmental Microbiology 55:11, 2909-2917.

Paduan, J. B., Zierenberg, R., Clague, D. A., Spelz, R. M., Caress, D. W., Troni, G., et al. 2018. Discovery of hydrothermal vent fields on Alarcón Rise and in southern Pescadero Basin, Gulf of California. *Geochemistry, Geophysics, Geosystems*, 19, 4788– 4819. doi.org/10.1029/2018GC007771

Peter, J.M., and Scott, S.D. 1988. Mineralogy, composition, and fluid-inclusion microthermometry of seafloor hydrothermal deposits in the southern trough of Guaymas Basin, Gulf of California. *Canadian Mineralogist* 26**,** 567-587.

Peterson, R.N., Burnett, W.C., Taniguchi, M., Chen, J., Santos, I.R., Ishitobi, T., 2008. Radon and radium isotope assessment of submarine groundwater discharge in the Yellow River delta, China. Journal of Geophysical Research 113. doi.org/10.1029/2008JC004776

Peterson, L. 2019. Evaluating fluid fluxes from deep-sea seepage habitats (Unpublished doctoral dissertation). Coastal Carolina University, Conway, SC, USA.

Portail, M., Olu, K., Esconbar-Briones, E., Caprais, J.C., Menot, L., Craud, P., Sarradin, P.M., Godfroy, A., and Sarrazin, J. 2015. Comparative study of vent and seep macrofaunal communities in the Guaymas Basin. Biogeosciences 12, 5455-5479, doi:10.5194/bg-12-5455-2015.

Portail, M., Olu, K., Dubois, S. F., Escobar-Briones, E., Gelinas, Y., Menot, L., and Sarrazin, J. 2016. Food-web complexity in Guaymas Basin hydrothermal vents and cold seeps, PLoSOne, 11,e0162263. doi.org/10.1371/journal.pone.0162263, 2016.

Rama, Moore, W.S., 1996. Using the radium quartet for evaluating groundwater input and water

exchange in salt marshes. Geochimica et Cosmochimica Acta 60, 4645–4652. doi.org/10.1016/S0016-7037(96)00289-X

Santos, Isaac R., Carlos Lechuga-Deveze, Richard N. Peterson, and William C. Burnett. Tracing Submarine Hydrothermal Inputs into a Coastal Bay in Baja California Using Radon. Chemical Geology 282.1-2 (2011): 1-10. doi.org/10.1016/j.chemgeo.2010.12.024

Schutte, C., A. Teske, B. MacGregor, V. Salman-Carvalho, G. Lavik, P. Hach, and D de Beer. 2018. Filamentous giant *Beggiatoaceae* from Guaymas Basin are capable of both denitrification and dissimilatory nitrate reduction to ammonium (DNRA). Applied and Environmental Microbiology 84: e02860-17. doi: 10.1128/AEM.02860-17.

Stein, C.A., Stein, S., 1994. Constraints on hydrothermal heat flux through the oceanic lithosphere from global heat flow. J. Geophys. Res., Solid Earth 99 (B2), 3081– 3095.
doi .org /10 .1029 /93JB02222.

Stein, C. A., S. Stein, and A. M. Pelayo, (1995). Heat flow and hydrothermal circulation, in *Seafloor Hydrothermal Systems: Physical, Chemical, Biological and Geological Interactions*, edited by S. E. Humphris, R. A. Zierenberg, L. S. Mullineaux, and R. E. Thomson, pp. 425–445, Geophysical Monograph 91, American Geophysical Union, Washington, DC. doi.org/10.1029/GM091p0425

Sun, Y., Torgersen, T., 1998. The effects of water content and Mn-fiber surface conditions on
^{224}Ra measurement by ^{220}Rn emanation. Marine Chemistry 62, 299–306. https://doi.org/10.1016/S0304-4203(98)00019-X

Takai, K., and Nakamura, K., 2010. Archaeal diversity and community development in deep-sea
hydrothermal vents. Current Opinion in Microbiology 14:3, 282-291.

Teske, A., Hinrichs, K.-U., Edgcomb, V., de Vera Gomez, A., Kysela, D., Sylva, S. P., Jannasch, H. W., 2002. Microbial Diversity of Hydrothermal Sediments in the Guaymas Basin: Evidence for Anaerobic Methanotrophic Communities. *Applied and Environmental Microbiology*, *68*(4), 1994. doi.org/10.1128/AEM.68.4.1994-2007.2002

Teske, A., Callaghan, A.V., LaRowe, D.E., 2014. Biosphere frontiers of subsurface life in the
sedimented hydrothermal system of Guaymas Basin. Frontiers in Microbiology 5. https://doi.org/10.3389/fmicb.2014.00362

Teske, A. and V. Salman. 2014. The family *Beggiatoaceae.* Chapter 6, pp. 93-134. In: The Prokaryotes – Gammaproteobacteria. DOI: DOI 10.1007/978-3-642-38922-

1_290. The Prokaryotes, 4th edition. Eugene Rosenberg, Edward F. DeLong, Fabiano Thompson, Stephen Lory, Erko Stackebrandt (Eds). Springer-Verlag, Berlin/Heidelberg.

Teske, A., de Beer, D., McKay, L., Tivey, M., Biddle, J., Hoer, D., Lloyd, K., Lever, M., Røy, H., Albert, D., Mendlovitz, H., Macgregor, B., 2016. The Guaymas Basin hiking guide to hydrothermal mounds, chimneys, and microbial mats: complex seafloor expressions of subsurface hydrothermal circulation. Frontiers in Microbiology 7:75, 1-23. doi:10.389/fmicb.2016.00075

Tivey, M.K, 1998. How to Build a Black Smoker Chimney. *Woods Hole Oceanographic Institution*, Oceanus Magazine.

Tivey, M.K. 2007. Generation of Seafloor Hydrothermal Vent Fluids and Associated Mineral Deposits. Oceanography. 20. doi.org/10.5670/oceanog.2007.80.

Von Damm, K. L., Edmond,J.M., Measures, C.I., and Grant B., 1985. Chemistry of submarine hydrothermal solutions at Guaymas Basin, Gulf of California, Geochim. Cosmochim. Acta, 49, 2221-2237.

Von Damm, K. L. 1995. Temporal and compositional diversity in seafloor hydrothermal fluids, *Rev. Geophys.*, 33(S2), 1297– 1305. doi.org/10.1029/95RG00283.

Tables

Table 1. Sediment core type and location of 16 cores sampled for this project during AT42-05.

Core ID	Latitude	Longitude	Date/Time Collected (EST)	Site	Core Depth (cmbsf)	In/Out Mat	Color
1	27.00796253	111.4072261	11/18/18 13:50	Aceto Balsamico	48	In	Yellow
2	27.00739528	111.4090454	11/19/18 16:40	Mat Mound	16	In	Orange
3	27.00640158	111.4076293	11/19/18 17:30	Mat Mound	45	Out	Orange
4	27.01123152	111.404445	11/20/18 15:28	Cathedral Hill	24	In	Yellow
5	27.0112103	111.4043553	11/20/18 15:07	Cathedral Hill	24	In	Orange
6	27.01118512	111.4043682	11/20/18 14:20	Cathedral Hill	12	In	White
7	27.01176175	111.4040113	11/21/18 13:59	Cathedral Hill	20	In	White
8	27.01170065	111.4040196	11/21/18 15:17	Cathedral Hill	20	In	White
9	27.00739122	111.4073225	11/23/18 15:54	Aceto Balsamico	28	In	White
10	27.00739122	111.4073225	11/23/18 16:00	Aceto Balsamico	28	In	White
11	27.00757417	111.4071248	11/24/18 13:07	Aceto Balsamico	20	In	Orange
12	27.00693733	111.4066294	11/24/18 10:43	Aceto Balsamico	16	Ref	NA
13	27.01146527	111.404494	11/25/18 11:14	Cathedral Hill	12	In	White
14	27.01181382	111.4038761	11/25/18 14:35	Cathedral Hill	32	In	Orange
15	27.01181382	111.4038761	11/25/18 14:42	Cathedral Hill	32	Out	Orange
16	27.01178973	111.4044134	11/26/18 13:35	Cathedral Hill	32	Ref	NA

Table 2. Summary of porewater volumes and in-situ porosity, with associated standard deviation, of sediments collected during AT42-05.

Core	AVG PW Volume (mL)	STD. Dev	AVG Porosity	STD. Dev
1	31.3	1.6	0.77	0.04
2	32.3	4.8	0.84	0.02
3	42.7	4.1	0.79	0.04
4	44.3	4.3	0.82	0.06
5	45.5	7.1	0.84	0.04
6	35.7	6.0	0.80	0.02
7	41.2	3.5	0.81	0.05
8	27.6	7.8	0.77	0.04
9	38.7	5.2	0.78	0.05
10	41.1	3.6	0.85	0.02
11	46.6	5.3	0.83	0.02
12	41.0	2.9	0.88	0.02
13	38.7	4.5	0.86	0.01
14	34.1	10.5	0.77	0.07
15	35.3	9.5	0.85	0.03
16	46.0	11.5	0.89	0.03
AVG All Cores:	**38.9**		**0.82**	
STD. Dev:	**5.5**		**0.04**	

Table 3. Summary of ^{224}Ra bottom water, surface layer activity, and whole core activity, with corresponding mat details, for 16 cores collected on AT42-05.

	Bottom Water		Surface Layer		Whole Core	
	AVG (dpm L^{-1})	Std Dev	AVG (dpm L^{-1})	Std Dev	AVG (dpm L^{-1})	Std Dev
All Mat:	11.2	9.8	41.9	32.1	30.1	13.4
Orange Mat:	9.5	9.1	60.0	46.7	25.8	14.3
White Mat:	10.2	8.6	28.9	12.1	34.3	12.5
Yellow Mat:	17.6	11.8	44.3	14.9	29.6	10.9
Reference:	0.6	0.0	0.9	0.8	3.4	0.9
Aceto Balsamico:	15.8	12.7	29.8	10.5	33.0	13.4
Mat Mound:	1.7	0.0	19.8	0.3	18.4	4.5
Cathedral Hill:	10.1	6.4	51.1	35.7	31.6	13.4

Table 4. Summary of ^{224}Ra surface layer equilibration activity and whole core activity, with corresponding mat details, for 16 cores collected on AT42-05.

	Surface Layer		Whole Core	
	AVG (dpm L⁻)	Std Dev	AVG (dpm L⁻¹)	Std Dev
All Mat:	28.8	34.2	21.0	13.0
Orange Mat:	54.6	49.5	26.6	17.5
White Mat:	14.2	4.8	20.1	9.1
Yellow Mat:	20.7	4.5	12.3	3.6
Reference:	1.9	0.4	13.5	1.7
Aceto Balsamico:	17.5	1.8	22.4	6.2
Mat Mound:	19.7	3.7	20.5	4.2
Cathedral Hill:	35.9	40.3	24.8	18.5

Table 5. Summary of the K_d and sediment core data sampled during AT42-05.

Core	AVG K_d	Location	Mat Presence (In/Out)	Mat Color
1	3.57 ± 0.58	AB	In	Yellow
2	1.55 ± 0.16	MM	In	Orange
3	1.76 ± 0.05	MM	Out	Orange
4	1.72 ± 0.71	CH	In	Yellow
5	0.94 ± 1.09	CH	In	Orange
6	0.84 ± 0.11	CH	In	White
7	2.22 ± 0.29	CH	In	White
8	1.69 ± 0.28	CH	In	White
9	3.35 ± 0.36	AB	In	White
10	2.06 ± 0.34	AB	In	White
11	2.43 ± 0.40	AB	In	Orange
12	3.16 ± 1.56	AB	Reference	NA
13	4.49 ± 1.13	CH	In	White
14	6.48 ± 2.48	CH	In	Orange
15	3.74 ± 1.22	CH	Out	Orange
16	1.66 ± 0.50	CH	Reference	NA

Table 6. ANOVA analysis comparing K_d, coring site, and mat presence/composition. Results indicate only 4% of the variance (η^2) in K_d is due to coring site or mat presence/composition.

ANOVA

Source of Variation	SS	df	MS	F	P-value	F crit
Between Groups	2.982254167	2	1.491127083	0.945498113	0.39607	3.20432
Within Groups	70.96864375	45	1.577080972			
Total	73.95089792	47				

Table 7. Summary of estimated flux rates for each core collected during AT42-05.

Core	Positive Flow (mL cm^{-2} d^{-1})	Std. Dev	Negative Flow (mL cm^{-2} d^{-1})	Std. Dev	In/Out Mat	Color	Location
1	3.35	1.34	8.04	2.37	In	Yellow	Aceto Balsamico
2	5.76	1.75	6.18	2.38	In	Orange	Mat Mound
3	2.78	0.76	4.94	4.77	Out	Orange	Mat Mound
4	0.00	0.00	3.93	1.01	In	Yellow	Cathedral Hill
5	3.11	1.36	1.70	0.87	In	Orange	Cathedral Hill
6	0.00	0.00	2.12	0.72	In	White	Cathedral Hill
7	2.39	1.01	1.45	0.81	In	White	Cathedral Hill
8	1.12	0.47	1.63	0.16	In	White	Cathedral Hill
9	2.29	1.24	0.00	0.00	In	White	Aceto Balsamico
10	4.43	1.32	4.72	1.45	In	White	Aceto Balsamico
11	2.36	1.04	7.10	3.86	In	Orange	Aceto Balsamico
12	0.00	0.00	20.07	5.21	Ref	NA	Aceto Balsamico
13	0.00	0.00	2.31	0.80	In	White	Cathedral Hill
14	1.21	0.84	4.29	4.03	In	Orange	Cathedral Hill
15	5.02	2.05	5.53	4.18	Out	Orange	Cathedral Hill
16	0.00	0.00	5.94	1.36	Ref	NA	Cathedral Hill

Table 8. Effective fluid flux rates for the top 16 cm of 14/16 cores collected during AT42-05. Core 15 was associated with high error in either +z or –z flow direction, and core 16 only yielded flow results in the bottom 16 cm of the core.

Fluid Flux Rates for top 16 cm of core

Core	Positive Flow (mL cm-2 d-1)	Std. Dev	Negative Flow (mL cm-2 d-1)	Std. Dev	In/Out Mat	Color	Location
1	3.35	1.34	-	-	In	Yellow	Aceto Balsamico
2	5.76	1.75	-	-	In	Orange	Mat Mound
3	2.78	0.76	-	-	Out	Orange	Mat Mound
4	-	-	3.93	1.01	In	Yellow	Cathedral Hill
5	-	-	1.70	0.87	In	Orange	Cathedral Hill
6	-	-	2.12	0.72	In	White	Cathedral Hill
7	2.39	1.01	-	-	In	White	Cathedral Hill
8	-	-	1.63	0.16	In	White	Cathedral Hill
9	2.29	1.24	-	-	In	White	Aceto Balsamico
10	-	-	4.72	1.45	In	White	Aceto Balsamico
11	2.36	1.04	-	-	In	Orange	Aceto Balsamico
12	-	-	20.07	5.21	Ref	NA	Aceto Balsamico
13	-	-	2.31	0.80	In	White	Cathedral Hill
14	1.21	0.84	-	-	In	Orange	Cathedral Hill

Table 9. Five casts within the Guaymas Basin were successfully captured and sampled for radium within active hydrothermal fluid flow. Table shows the bottom ~100 m of the 5 successful casts in Guaymas Basin, the Pescadero cast, and the control cast. Time restrictions did not allow for a control cast to be collected in the Pescadero Basin.

CCU Sample ID	Cruise Event #	Vent Site	Depth (m)	Temperature (ITS90 °C)	Ra-224 (dpm/L)	Unc (dpm/L)
WC 4-1	3.002	Big Pagoda	1975	4.5	0.03	0.00
WC 4-2	3.002	Big Pagoda	1970	3.0	0.13	0.01
WC 4-3	3.002	Big Pagoda	1965	3.3	0.34	0.02
WC 4-4	3.002	Big Pagoda	1955	3.0	0.11	0.01
WC 4-5	3.002	Big Pagoda	1930	2.9	0.02	0.00
WC 4-6	3.002	Big Pagoda	1880	2.9	0.01	0.00
WC 8-1	8.001	Alvin Spire	1891	2.9	0.00	0.00
WC 8-2	8.001	Alvin Spire	1941	2.9	0.00	0.00
WC 8-3	8.001	Alvin Spire	1966	2.9	0.01	0.00
WC 8-4	8.001	Alvin Spire	1985	2.9	0.03	0.00
WC 8-5	8.001	Alvin Spire	1991	3.5	0.08	0.01
WC 9-1	10.002	Falkor's Fountain	1878	2.9	0.00	0.00
WC 9-2	10.002	Falkor's Fountain	1928	2.9	0.00	0.00
WC 9-3	10.002	Falkor's Fountain	1953	2.9	0.01	0.00
WC 9-4	10.002	Falkor's Fountain	1973	2.9	0.01	0.00
WC 9-5	10.002	Falkor's Fountain	1978	3.0	0.11	0.01
WC 10-1	11.003	Control	1803	2.6	0.00	0.00
WC 10-2	11.003	Control	1853	2.6	0.00	0.00
WC 10-3	11.003	Control	1878	2.6	0.00	0.00
WC 10-4	11.003	Control	1898	2.6	0.00	0.00
WC 10-5	11.003	Control	1903	2.6	0.01	0.00
WC 12-1	13.001	Big Pagoda	1671	2.9	0.00	0.00
WC 12-2	13.001	Big Pagoda	1921	2.9	0.02	0.00
WC 12-3	13.001	Big Pagoda	1961	3.0	0.01	0.00
WC 12-4	13.001	Big Pagoda	1966	3.9	0.37	0.03
WC 12-5	13.001	Big Pagoda	1971	5.4	0.36	0.03
WC 13-1	14.001	Pescadero	3640	1.9	0.00	0.00
WC 13-2	14.001	Pescadero	3655	2.5	0.19	0.01
WC 13-3	14.001	Pescadero	3659	5.6	1.37	0.10

Figures
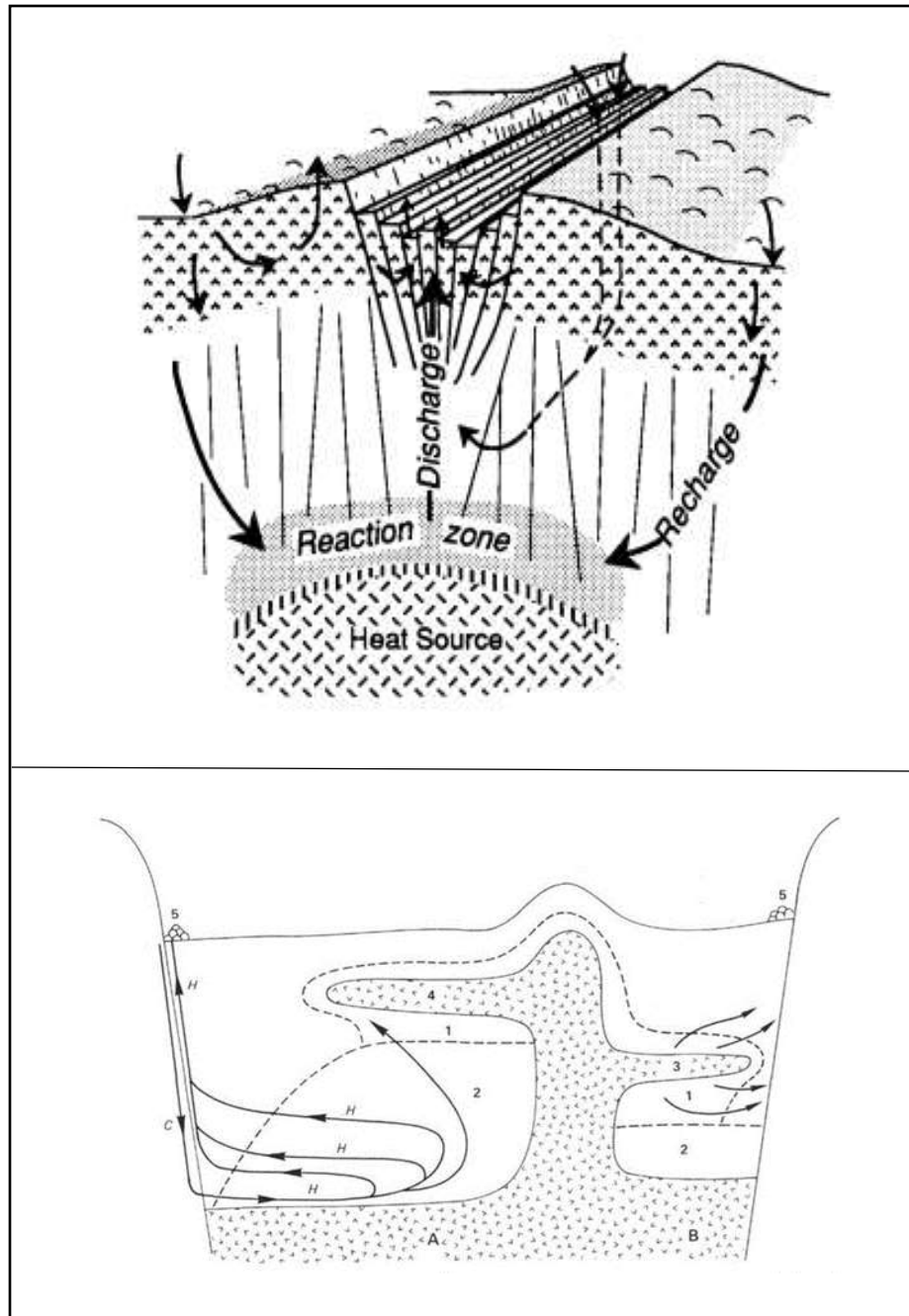
Figure 1. Diagram illustrating the process of recharge and discharge along MORs (top panel; Alt, 1995). Diagram illustrating potential circulation pathways specifically in Guaymas Basin, Gulf of California, where "H" represents hot, venting fluid and "C" represents cold, advected bottom water, and "3 & 4" represent basaltic sill intrusions (bottom panel; Gieskes et al., 1982).
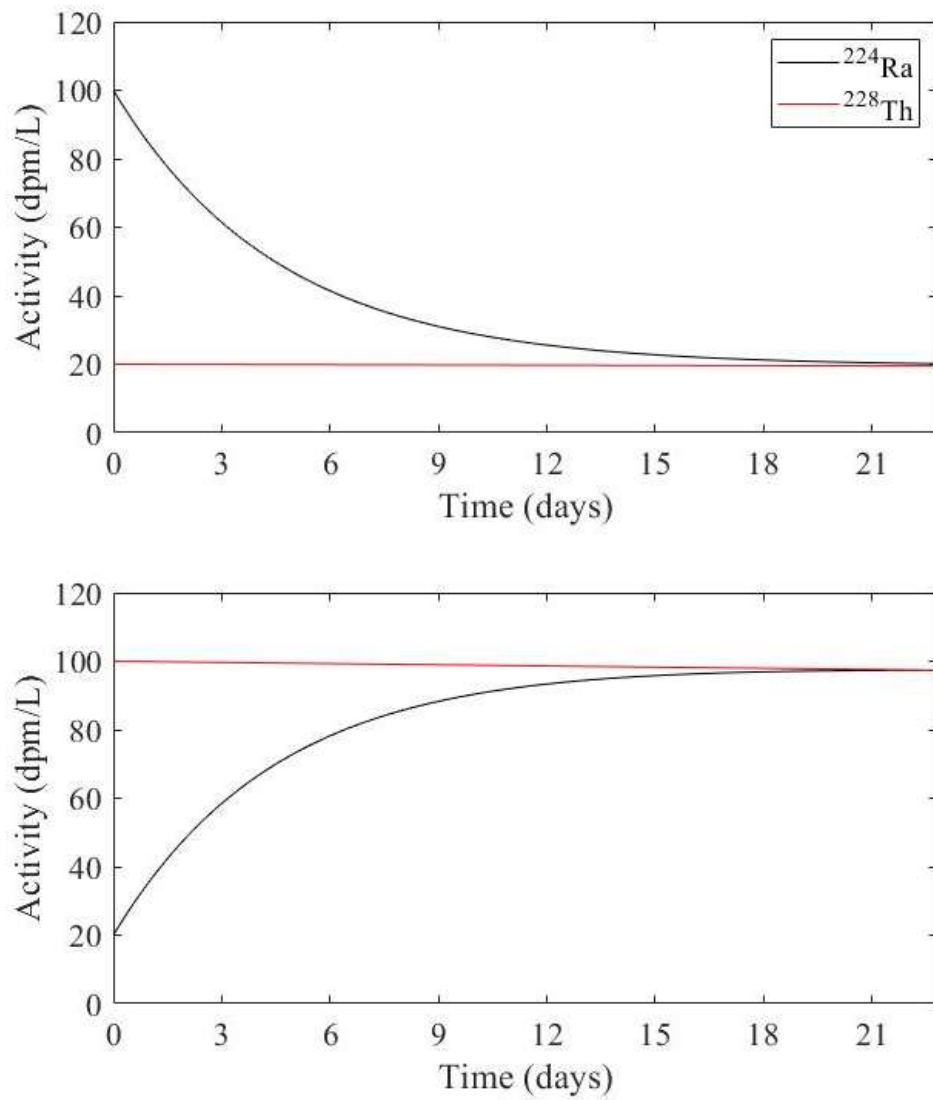
Figure 2. Theoretical ingrowth (bottom) and decay (top) curves of ^{224}Ra to its ^{228}Th parent. Three weeks of incubation allows the ^{224}Ra to go through approximately 6 half-lives in order to approach secular equilibrium with the ^{228}Th.
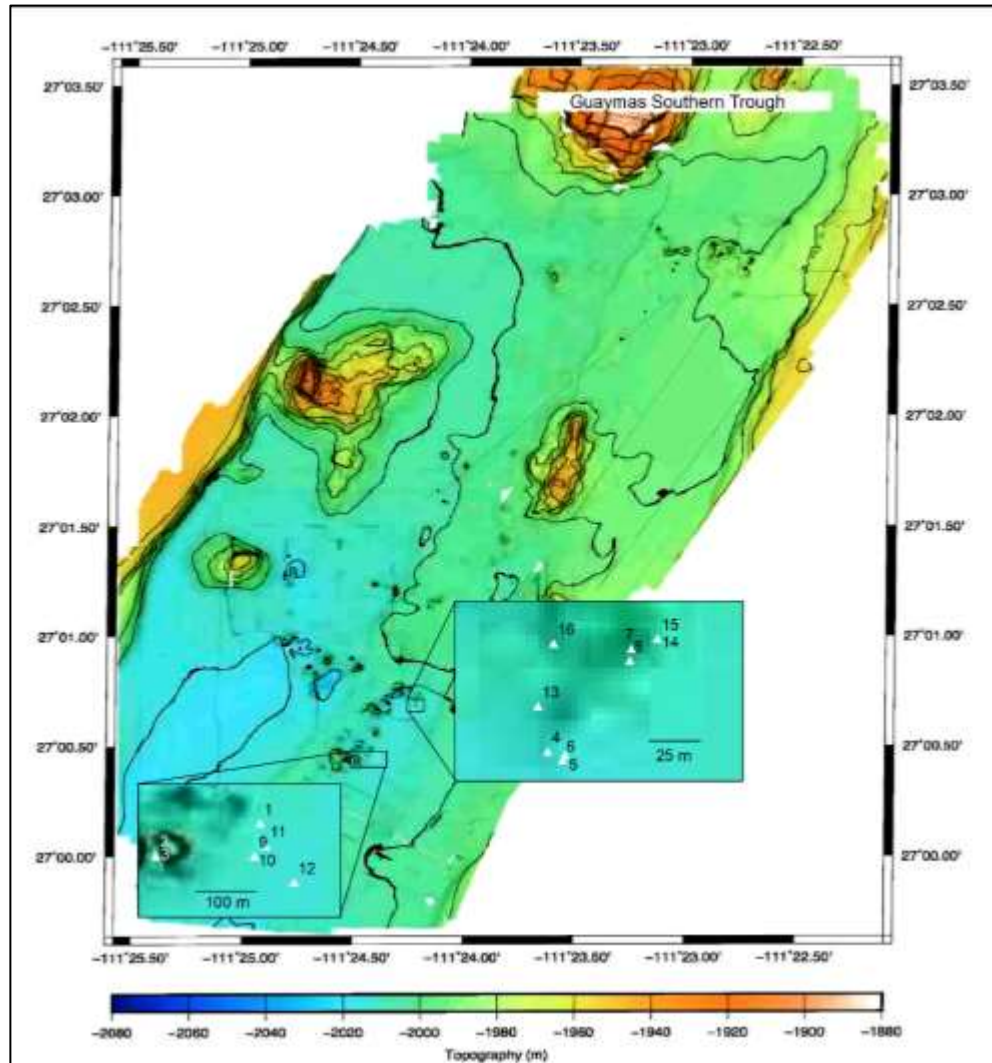
Figure 3. Sample map of 16 sediment cores collected on AT42-05 in November 2018 onboard the R/V Atlantis in Guaymas Basin, Gulf of California, Mexico, on Sentry bathymetric data collected in 2016 (Teske at al., 2016).
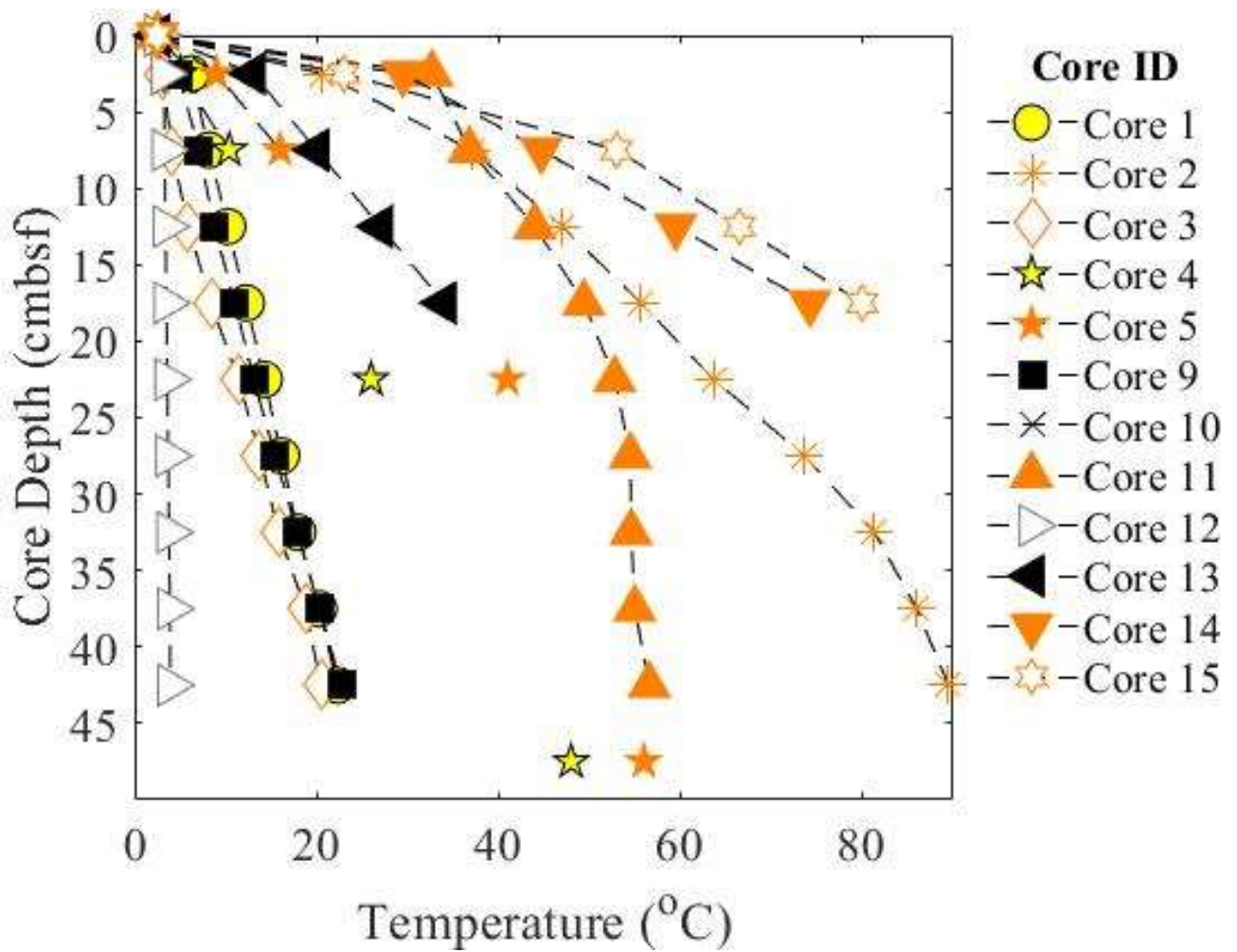
Figure 4. A plot of temperature versus depth down the core for 12 of 16 cores with recorded temperature data collected on AT42-05. Open faces represent cores collected just outside of a mat and filled symbols represent cores collected inside of a mat. Orange symbols represent orange bacterial mat presence, yellow represents yellow bacterial mat presence, and black symbols represent white bacterial mat presence. Open, grey triangles represent background sediment.
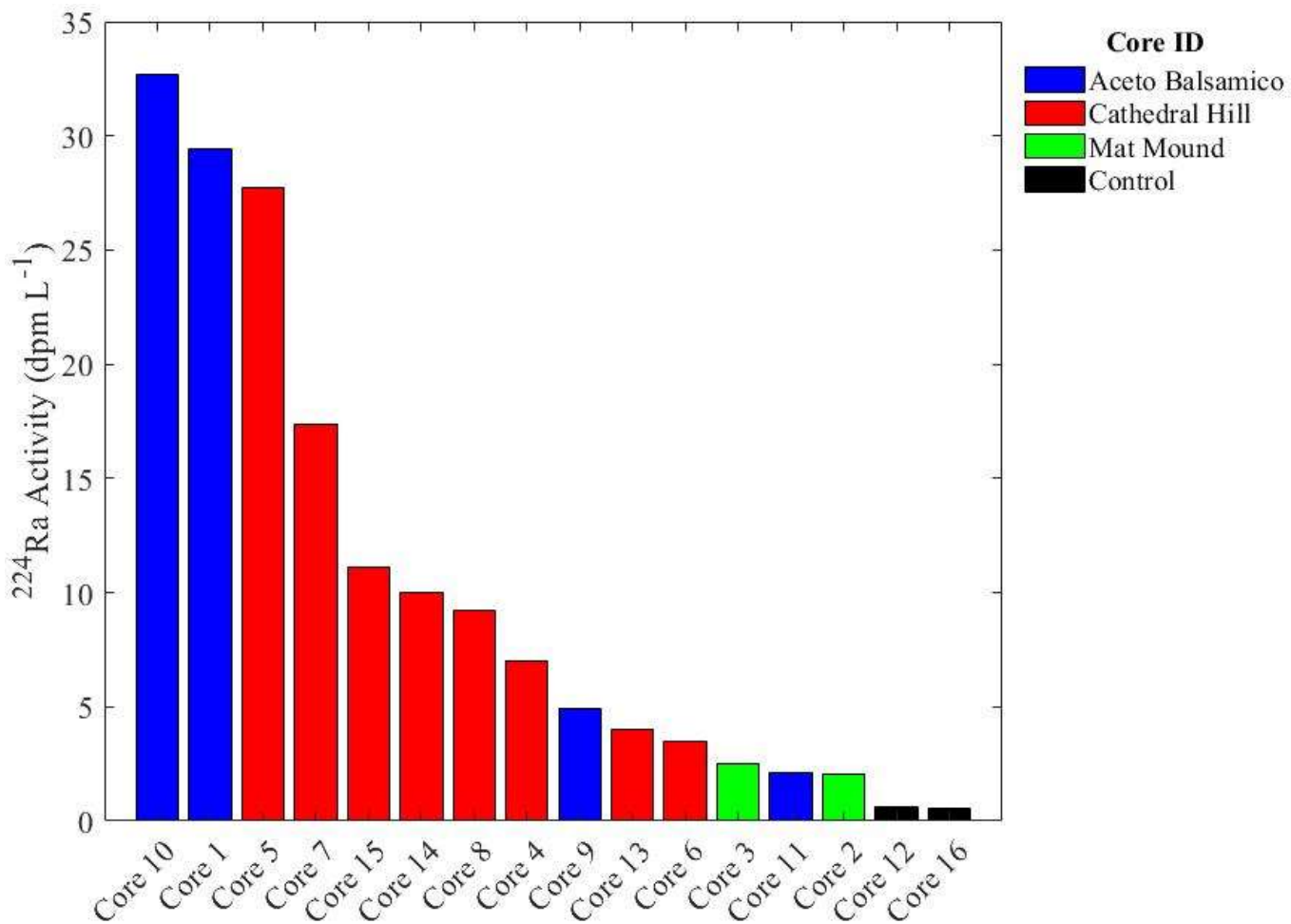
Figure 5. Bottom water ^{224}Ra activity for sixteen sediment cores collected on AT42-05.
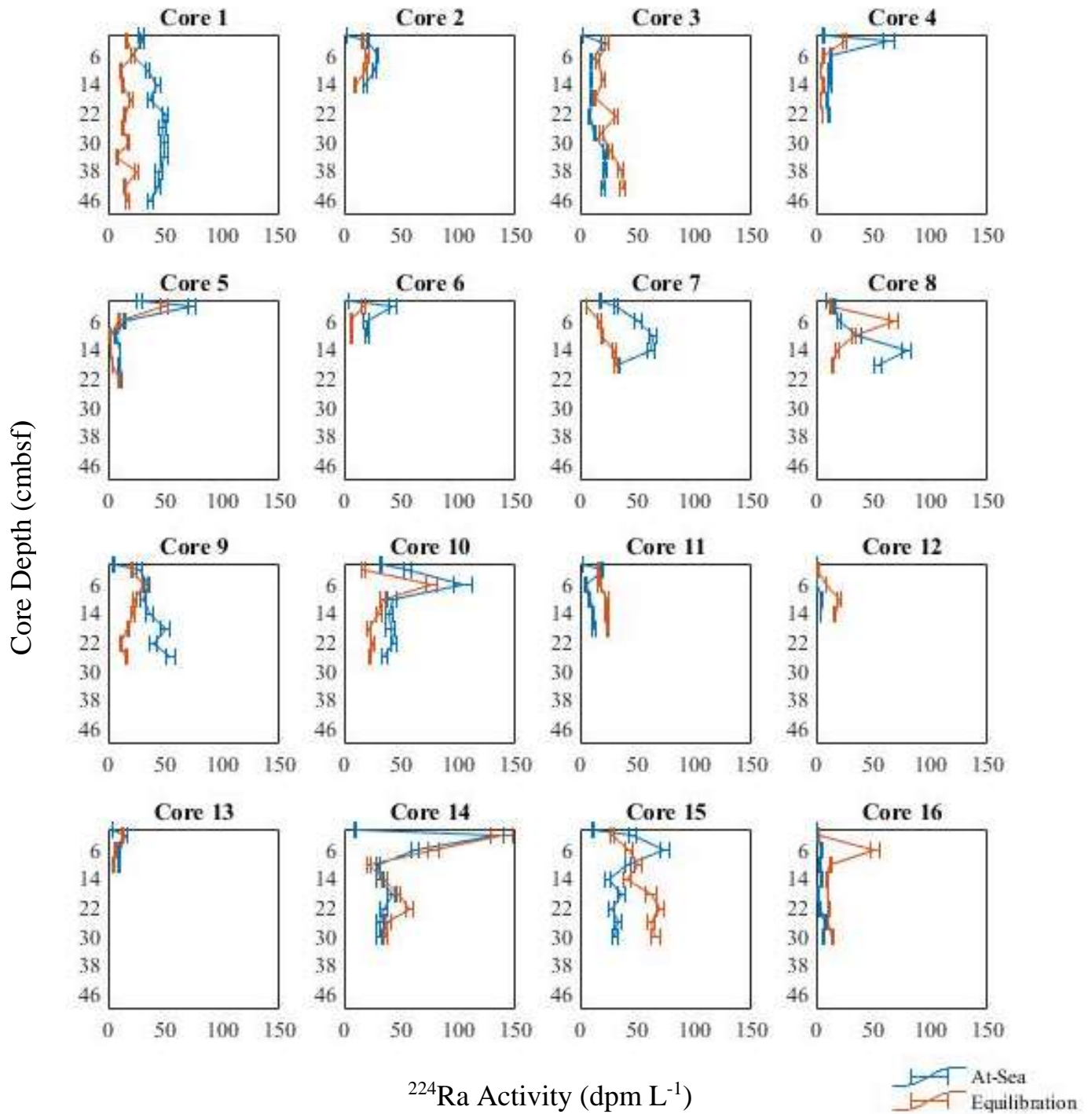
Figure 6. ^{224}Ra activities measured at-sea and after equilibration experiments, with bottom water activities included in at-sea measurements. Axes are standardized for purposes of comparison.
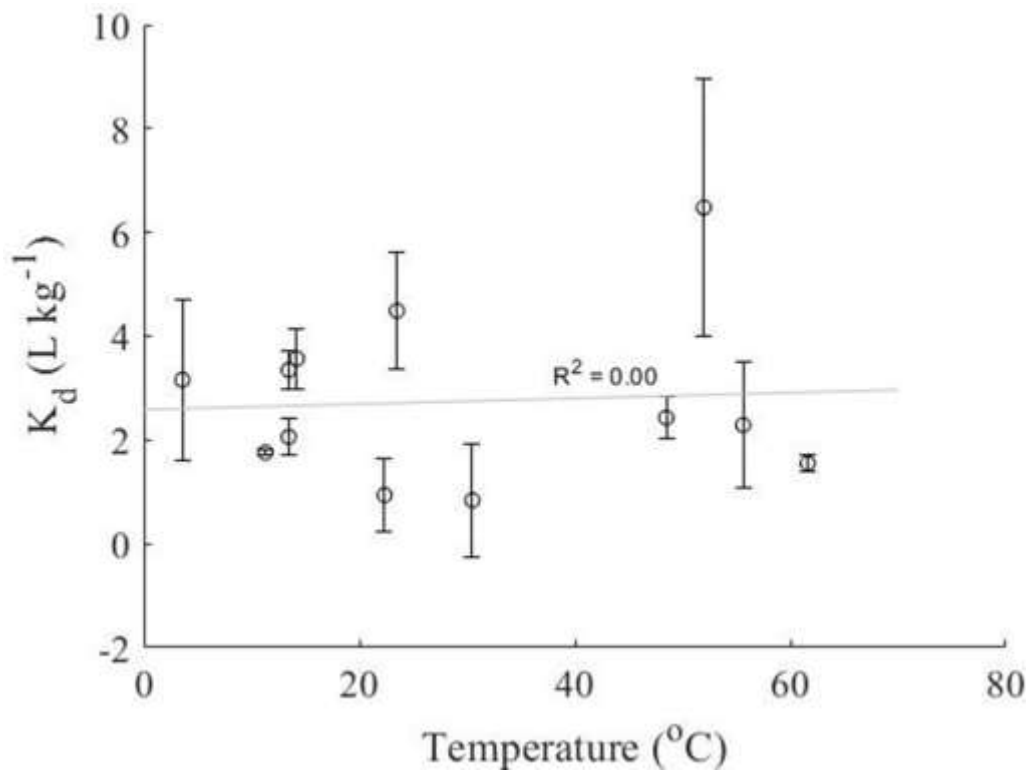
Figure 7. K_d versus Average Temperature of 12 cores with temperature data taken on AT42-05.
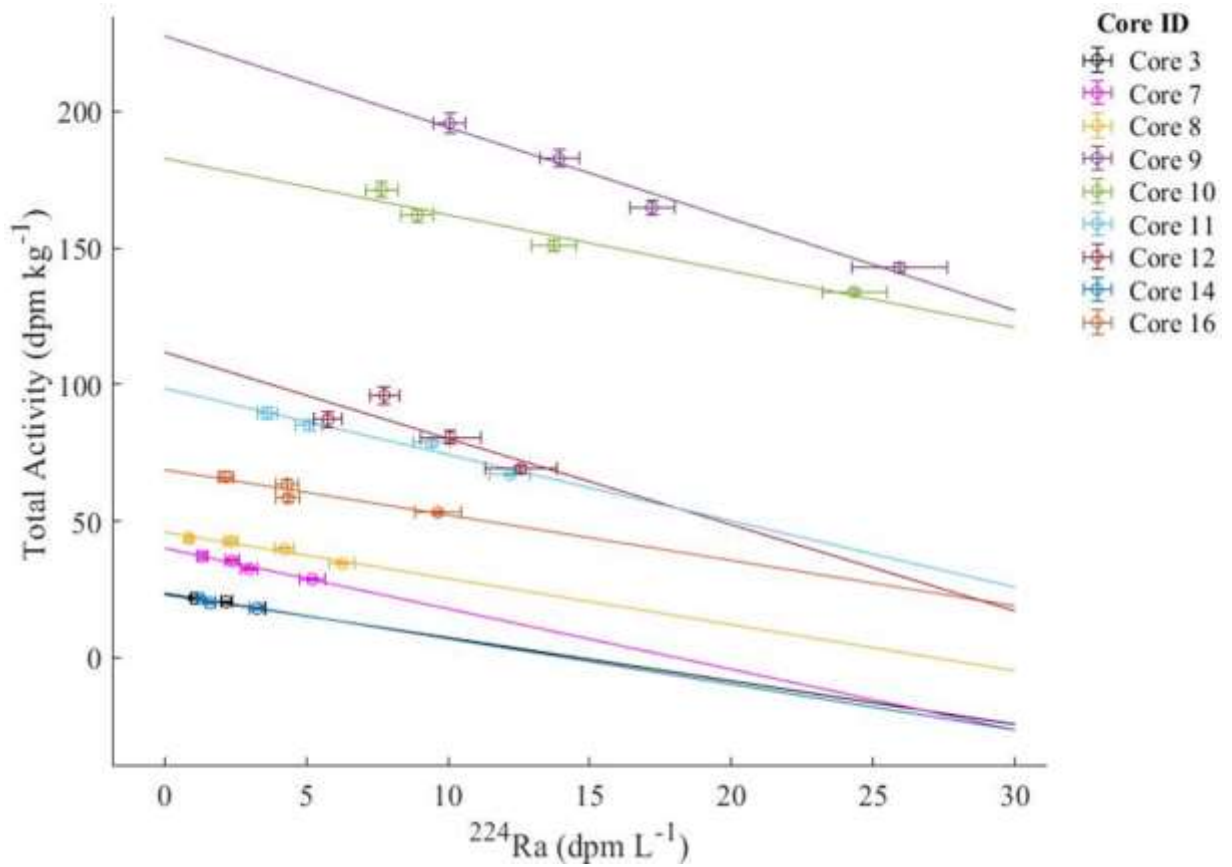
Figure 8. Results of K_d serial extraction experiments of layer 4 (16 to 20 cmbsf) for all nine cores that followed expected trends, with linear regression lines. The results demonstrate what we expected to see in depleting activity over the course of the experiment.
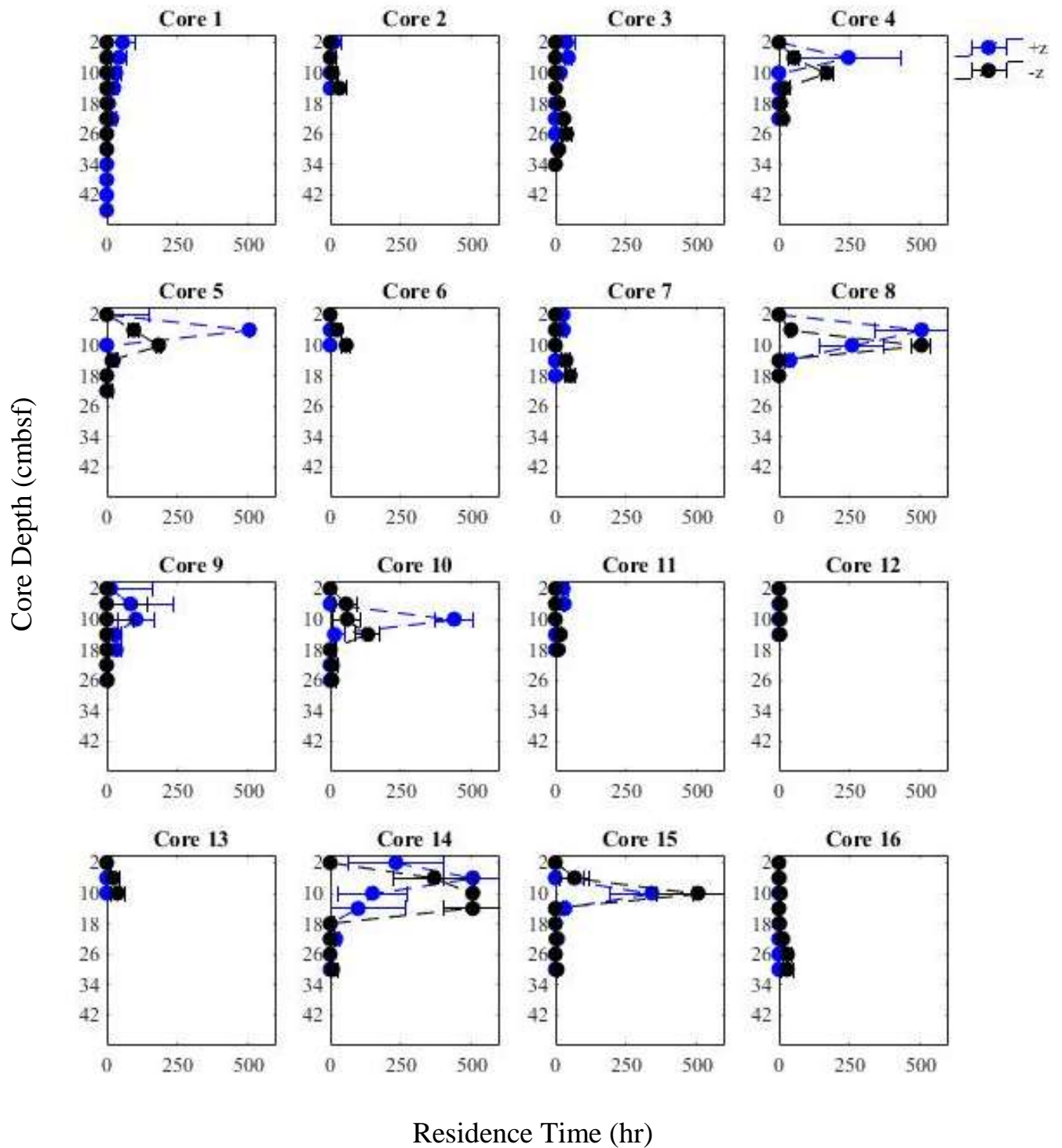
Figure 9. Pore fluid residence time down core for both recharge (-z) and discharge (+z) flow directions. Error in cores 8, 14, and 15 exceeded resolvable residence time (>21 days). Axes are standardized for purposes of comparison.
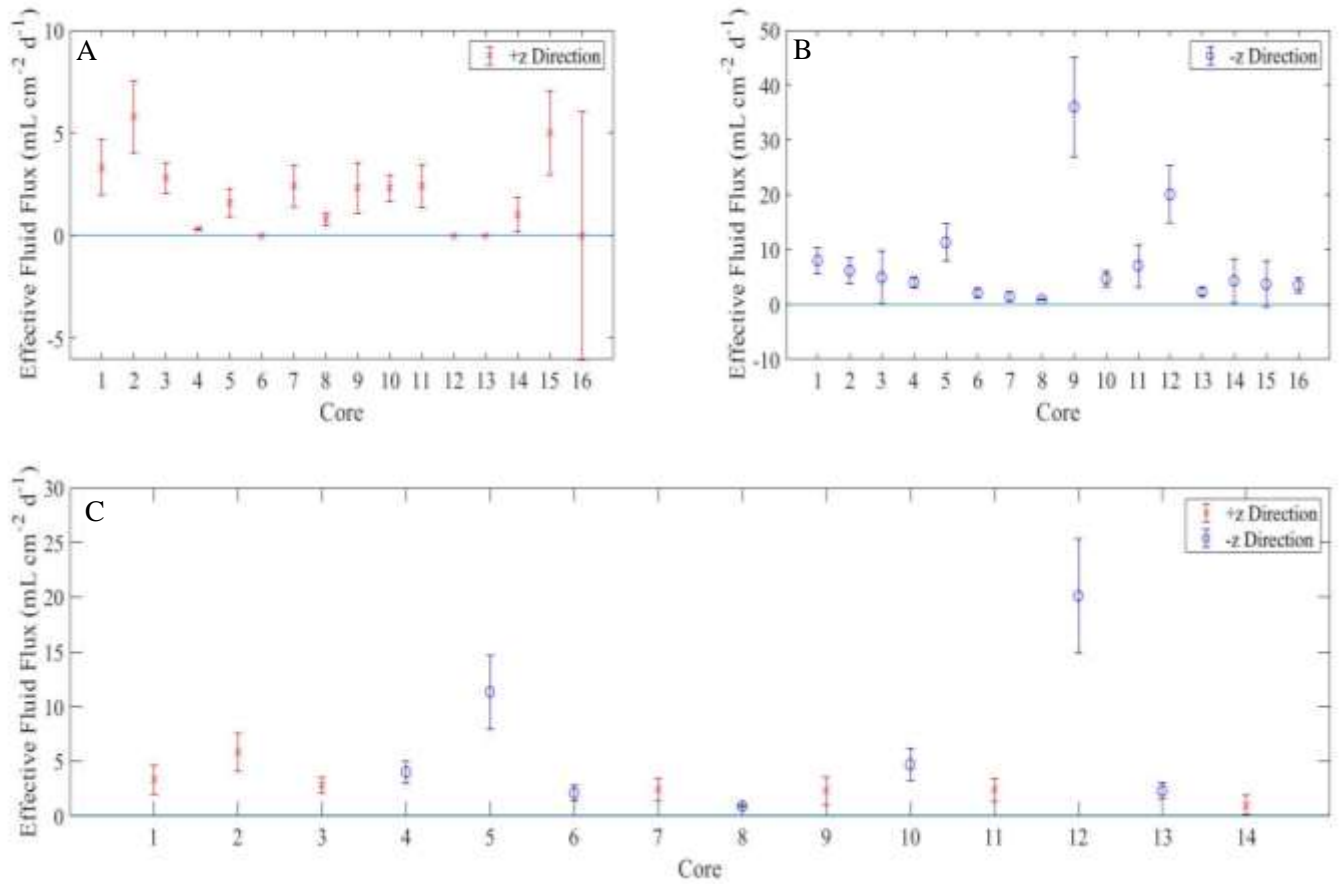
Figure 10. Fluid flux profiles of cores collected from AT42-05. **(A).** Potential effective fluid flux for all cores, averaged over the whole core, in the +z direction. **(B).** Potential effective fluid flux for all cores, averaged over the whole core, in the downward direction. **(C).** Likely effective fluid flux for cores 1-14 in the top 16 cm of the core. Core 15 could not be resolved in either flow direction. Core 16 only yielded a solution for –z flow in the bottom of the core (22-30 cm).
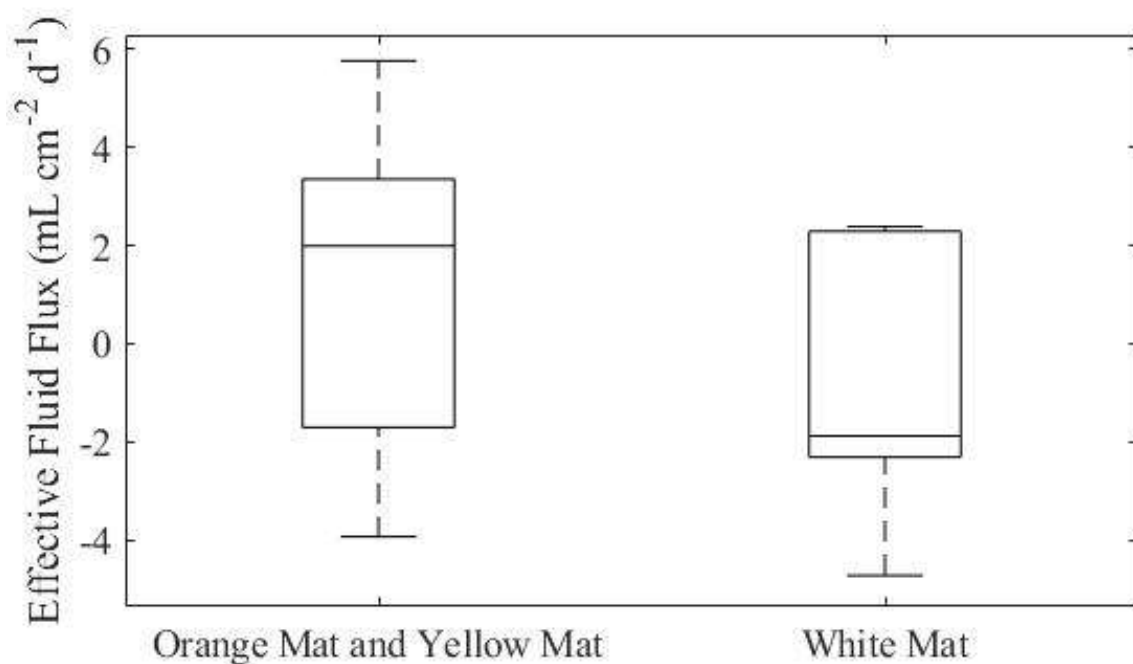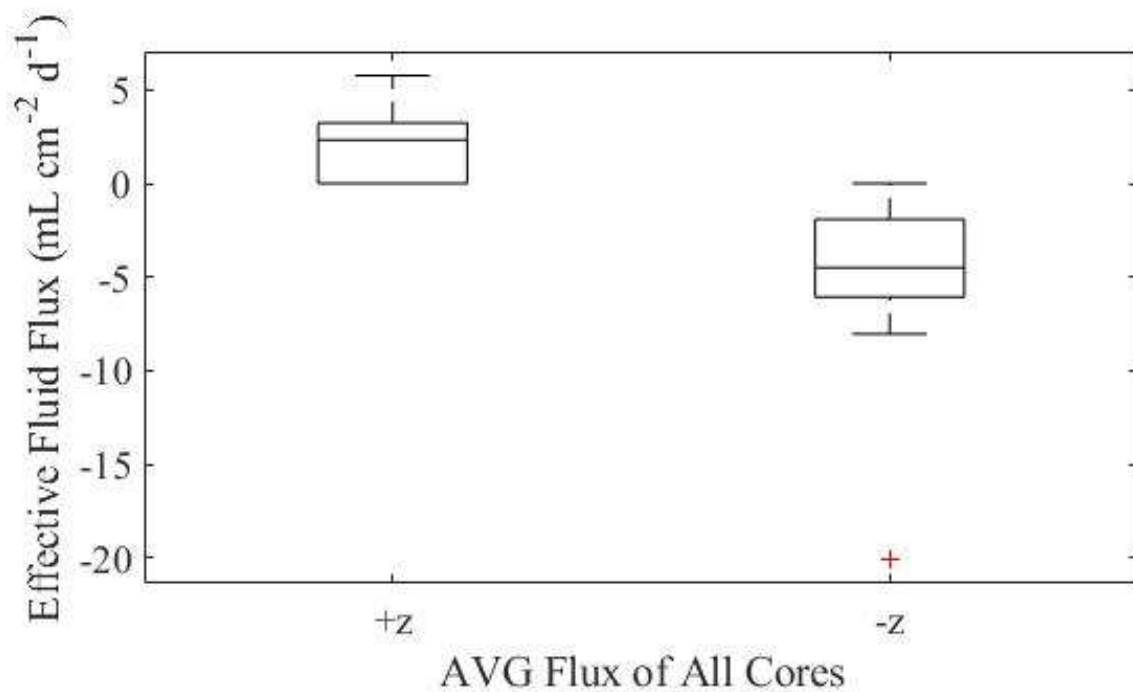
Figure 11. Average effective fluid flux for all cores collected on AT42-05 (top) where +z is in the upward direction and –z is in the downward direction. Average effective fluid flux for cores collected within microbial mat cores on AT42-05 (bottom).
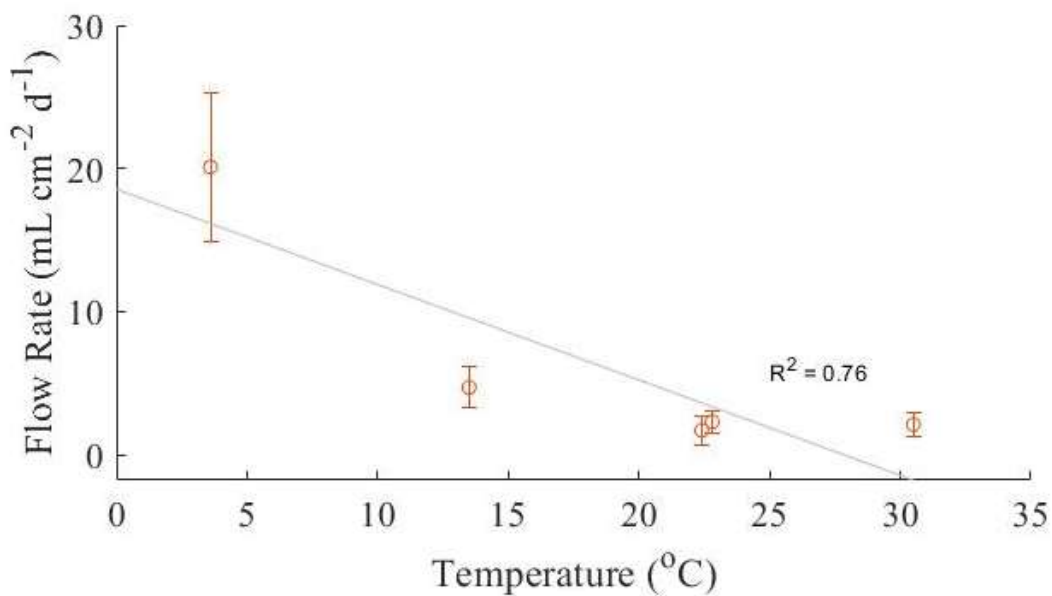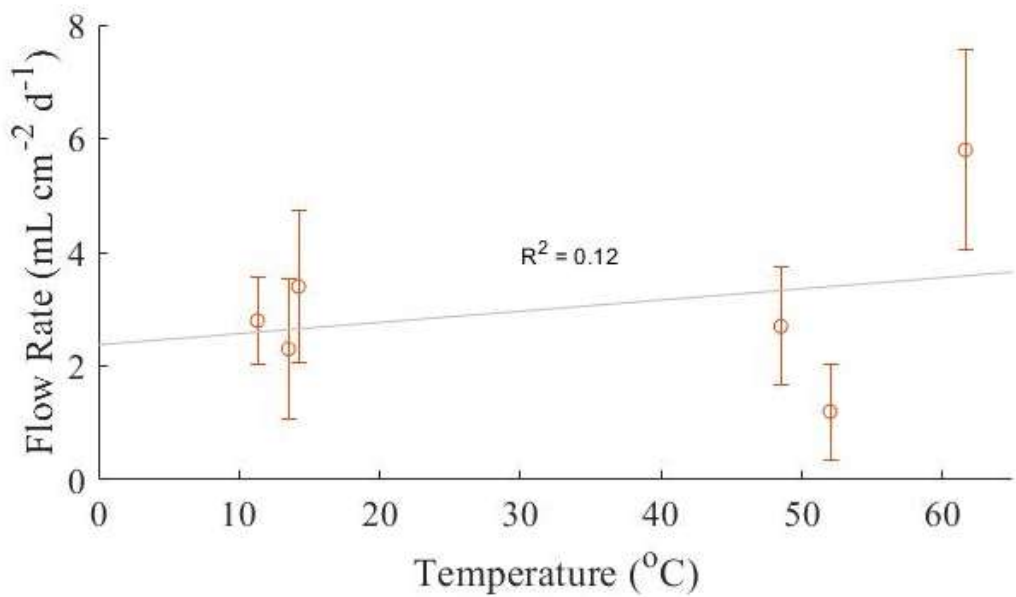
Figure 12. Plot of effective fluid flux in the top 16 cm of a core vs average temperature for 11 cores collected on AT42-05. Top Panel: Positive fluid flux results. Bottom: Negative fluid flux results. Five cores were omitted due to missing temperature data and/or fluid flux rates that did not yield a solution.
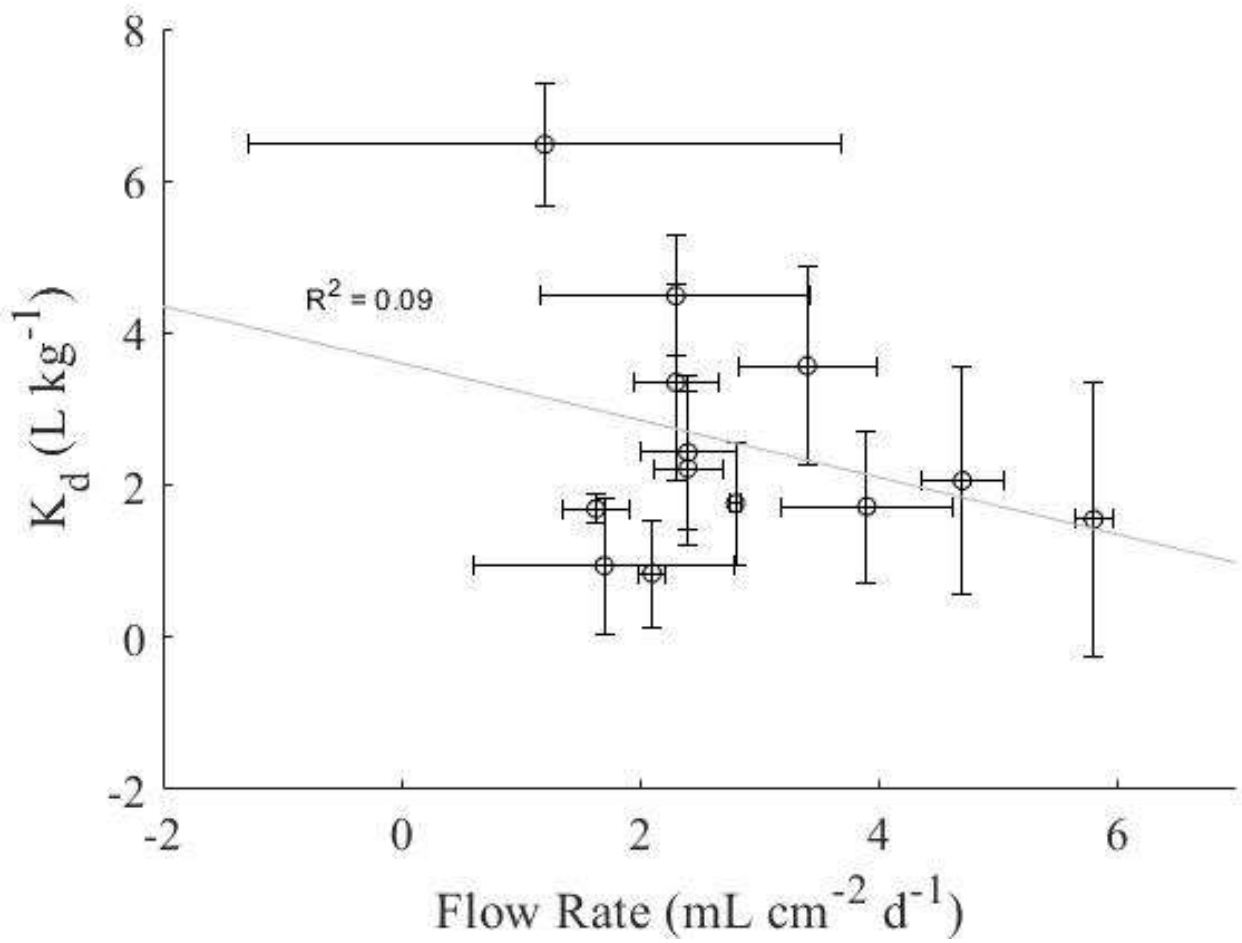
Figure 13. Plot of K_d versus Fluid Flux for 16 sediment cores collected on AT42-05.
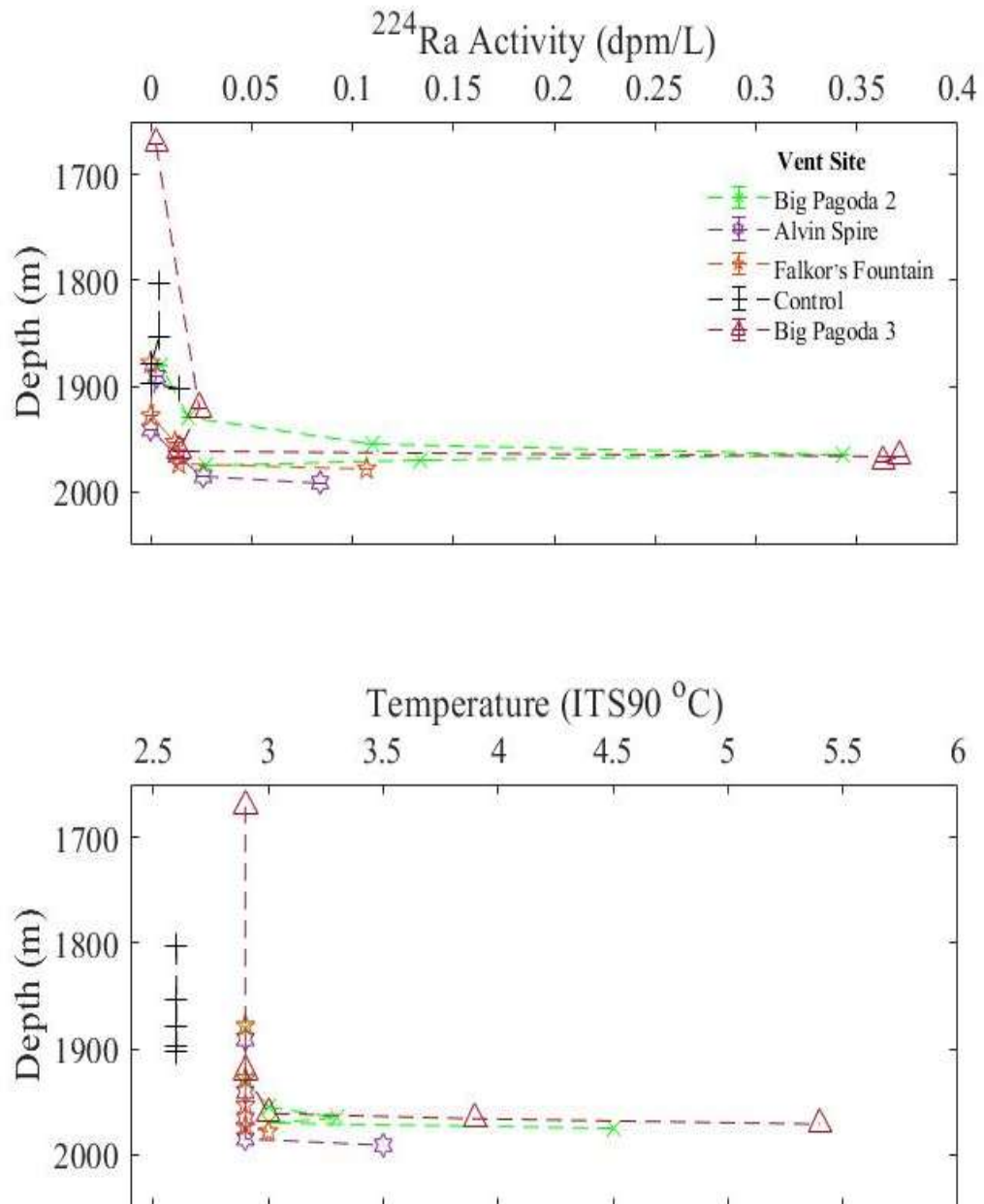
Figure 14. Water column 224Ra activity and associated temperature data from Guaymas Basin collected on cruise FK190211.
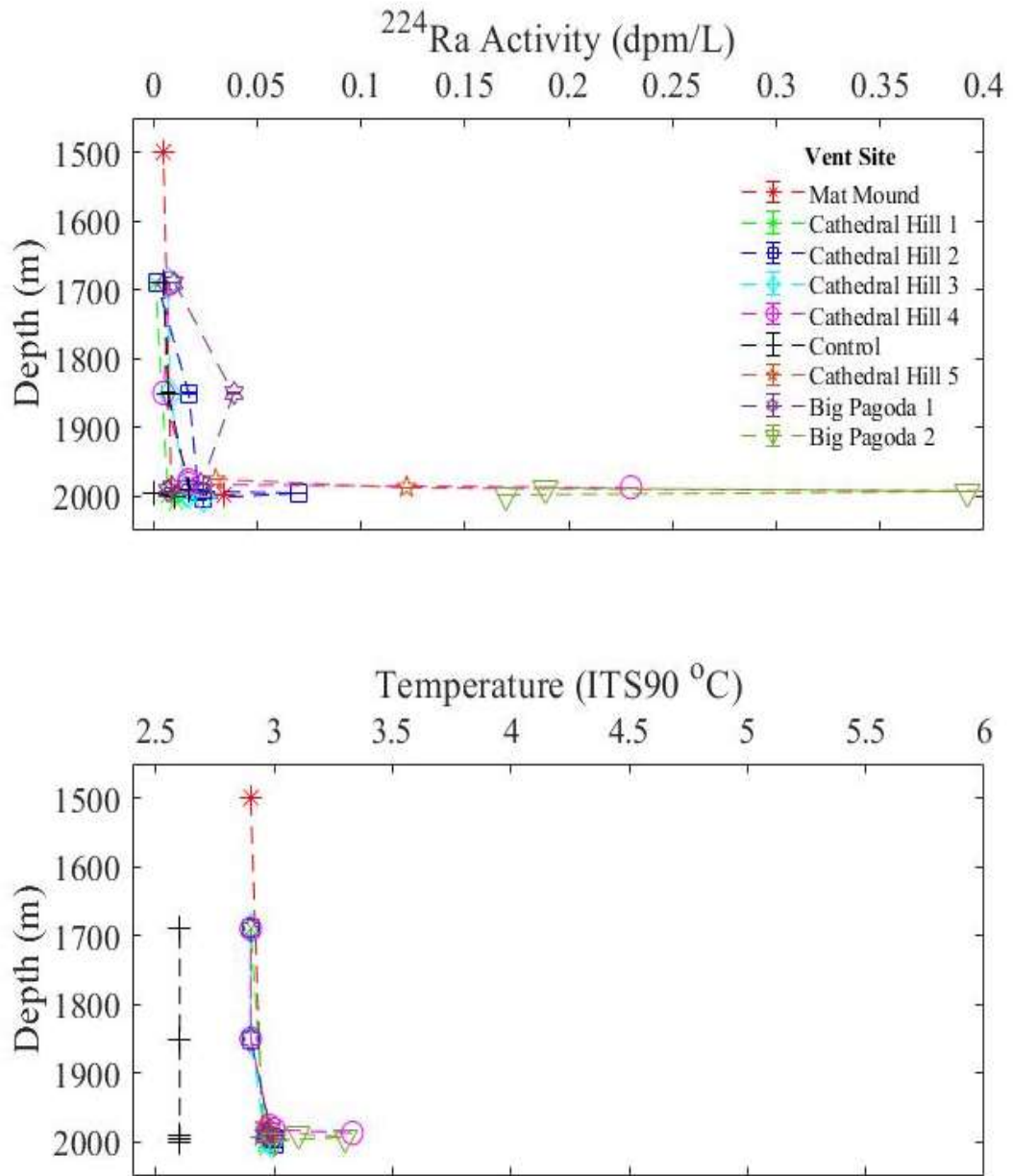
Figure 15. Water column 224Ra activity and associated temperature data from Guaymas Basin collected on cruise AT42-05.
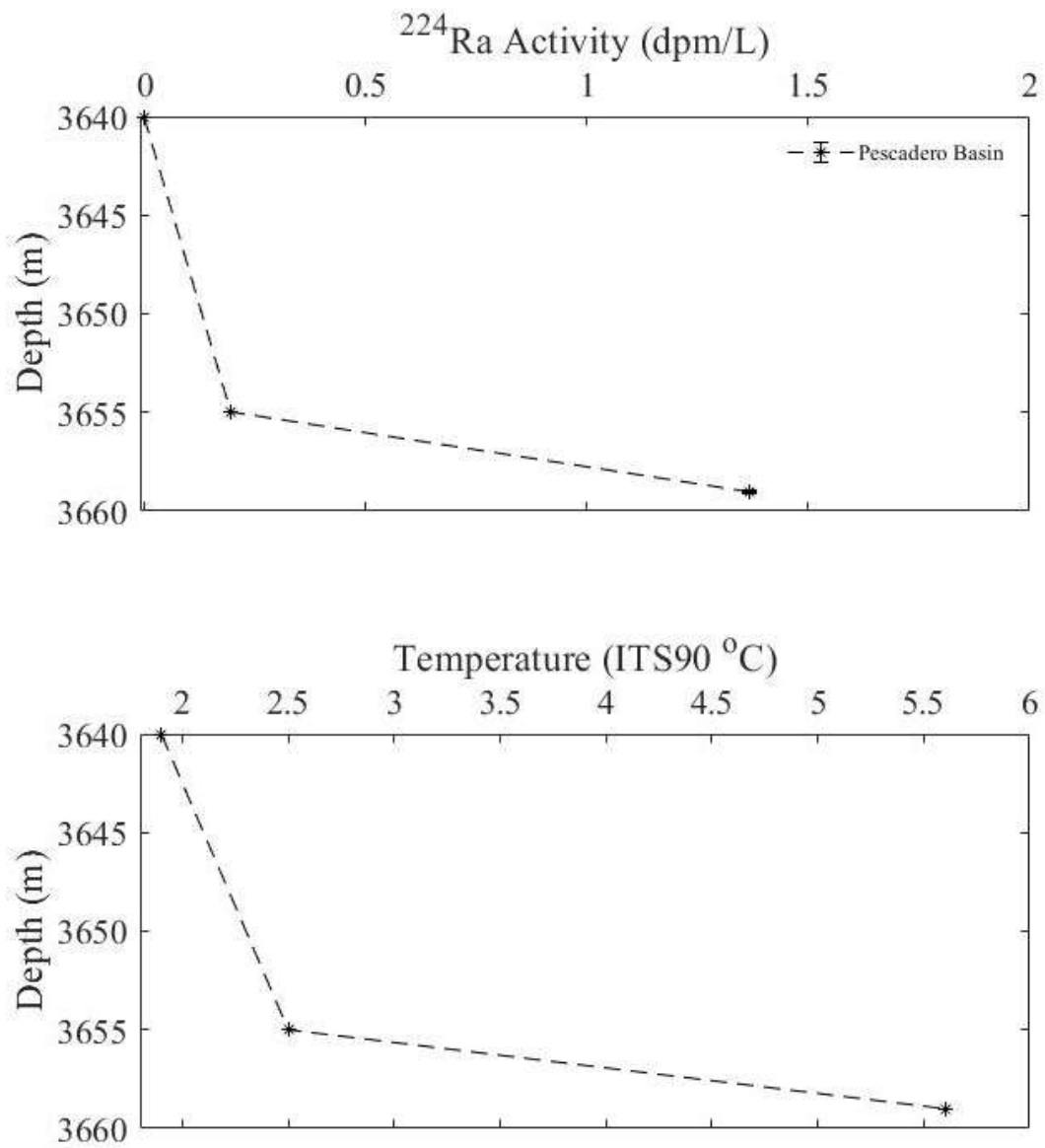
Figure 16. Water column 224Ra activity and associated temperature data from the Pescadero sample site collected on cruise FK190211.
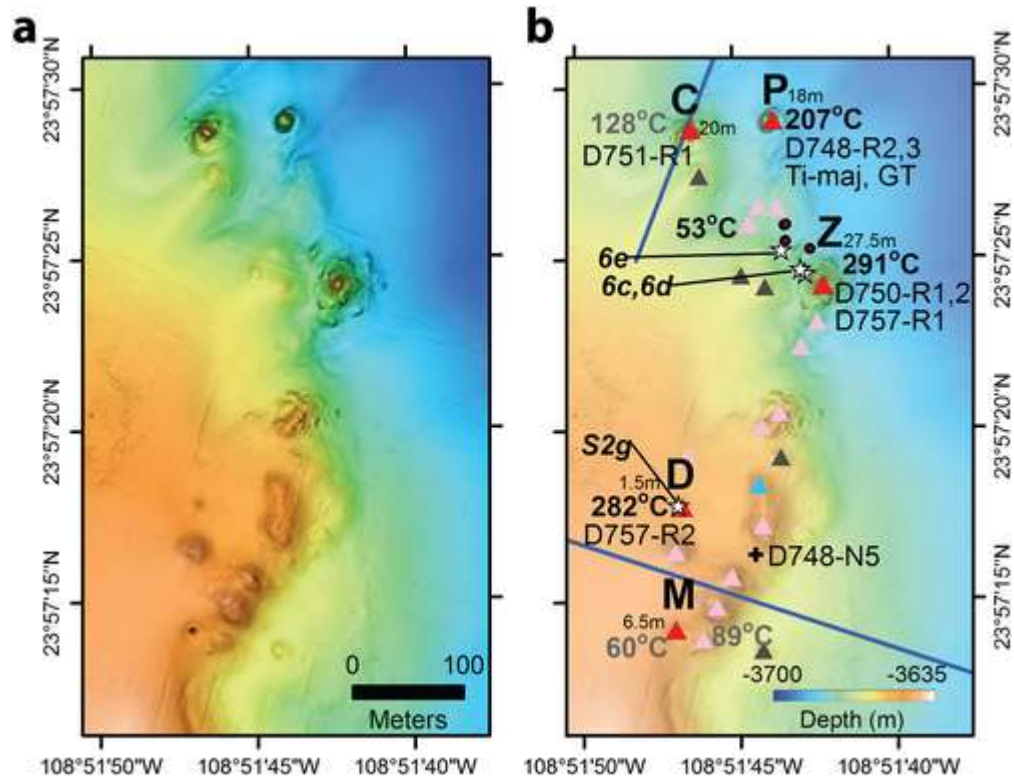
Figure 17. Sample sites identified in Paduan et al. (2015). Site 'Z' venting chimney is likely the same site sampled on FK190211, and was identified in 2015 as a chimney along the Pescadero Transform Fault.

APPENDIX I: Metadata

AT42-05 Core Sample Metadata

Sample ID	Dive Number	CCU Core ID	Latitude	Longitude	Date/Time Collected (EST)	Site	Core Depth (cmbsf)	In/Out Mat	Color
AB 44	4992	1	27.00796253	111.4072261	11/18/18 13:50	Aceto Balsamico	48	In	Yellow
MM 14	4993	2	27.00739528	111.4090454	11/19/18 16:40	Mat Mound	16	In	Orange
MM 31	4993	3	27.00739528	111.4090454	11/19/18 17:30	Mat Mound	45	Out	Orange
CH 15	4994	4	27.01123152	111.404445	11/20/18 15:28	Cathedral Hill	24	In	Yellow
CH 21	4994	5	27.0112103	111.4043553	11/20/18 15:07	Cathedral Hill	24	In	Orange
CH 23	4994	6	27.01118512	111.4043682	11/20/18 14:20	Cathedral Hill	12	In	White
CH 4	4997	7	27.01176175	111.4040113	11/21/18 13:59	Cathedral Hill	20	In	White
CH 6	4997	8	27.01170065	111.4040196	11/21/18 15:17	Cathedral Hill	20	In	White
AB 39	4998	9	27.00739122	111.4073225	11/23/18 15:54	Aceto Balsamico	28	In	White
AB 45	4998	10	27.00739122	111.4073225	11/23/18 16:00	Aceto Balsamico	28	In	White
AB 7	4999	11	27.00757417	111.4071248	11/24/18 13:07	Aceto Balsamico	20	In	Orange
AB 16	4999	12	27.00693733	111.4066294	11/24/18 10:43	Aceto Balsamico	16	Ref	NA
CH 2	5000	13	27.01146527	111.404494	11/25/18 11:14	Cathedral Hill	12	In	White
CH 39	5000	14	27.01181382	111.4038761	11/25/18 14:35	Cathedral Hill	32	In	Orange
CH 41	5000	15	27.01181382	111.4038761	11/25/18 14:42	Cathedral Hill	32	Out	Orange
CH 39B	5001	16	27.01178973	111.4044134	11/26/18 13:35	Cathedral Hill	32	Ref	NA
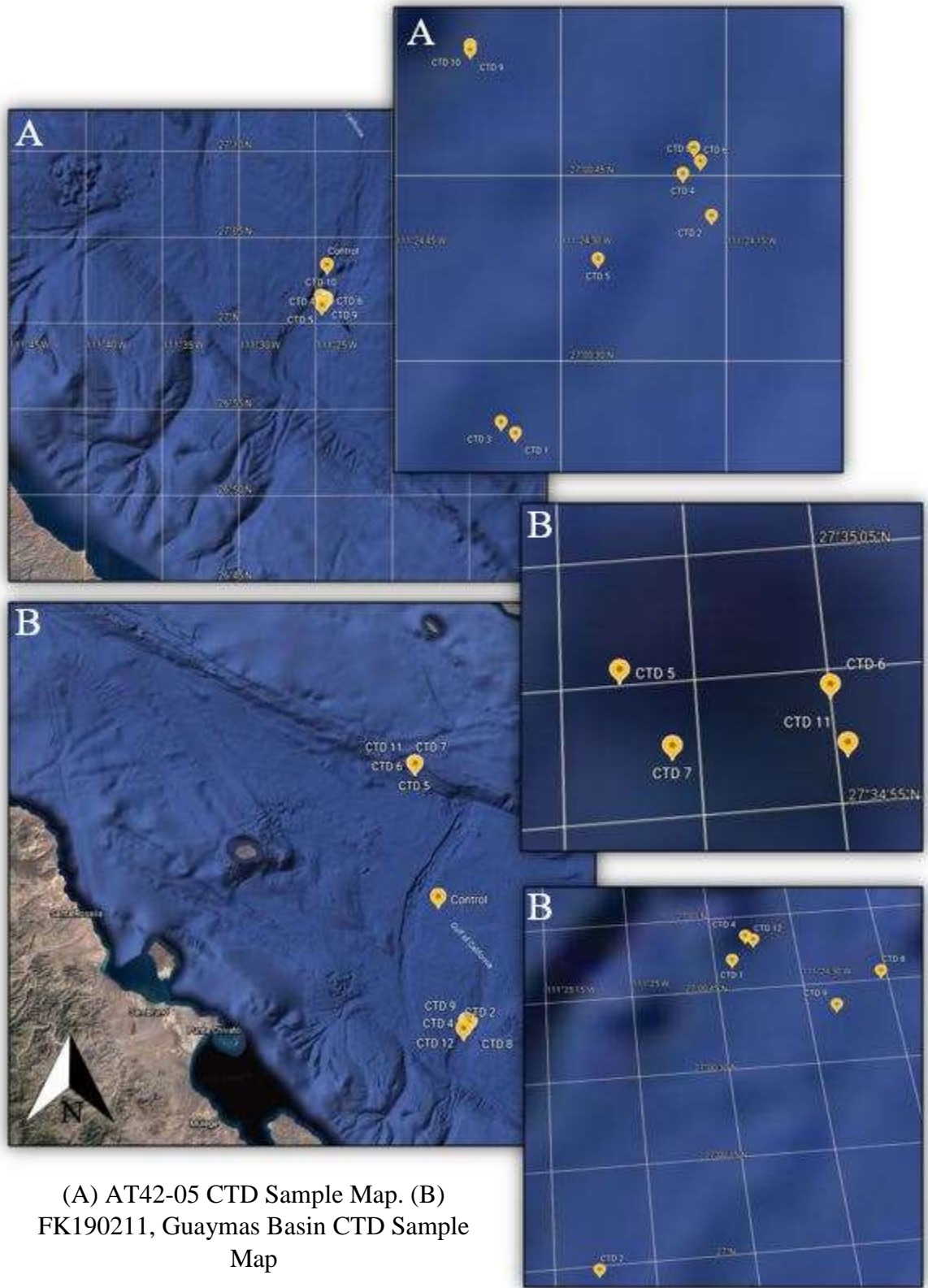
(A) AT42-05 CTD Sample Map. (B)
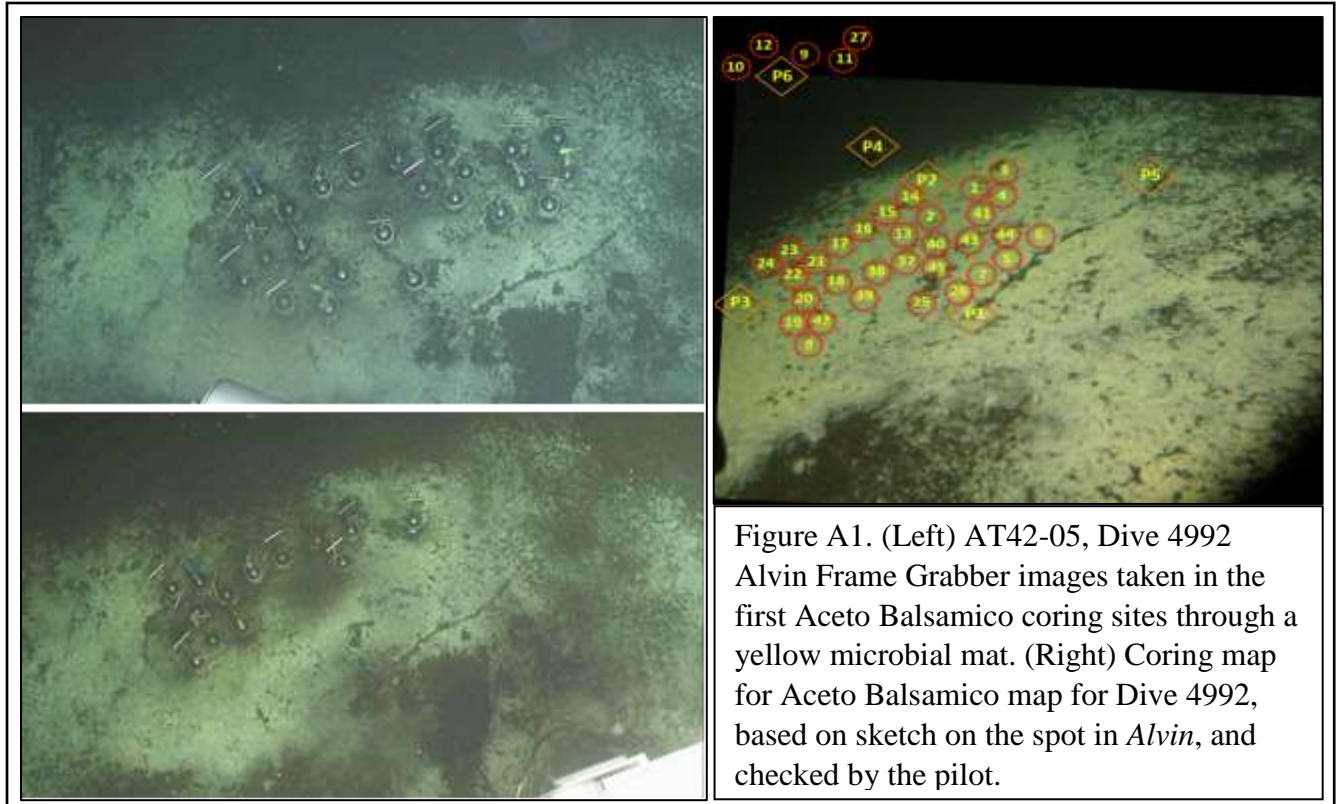FK190211, Guaymas Basin CTD Sample
Map

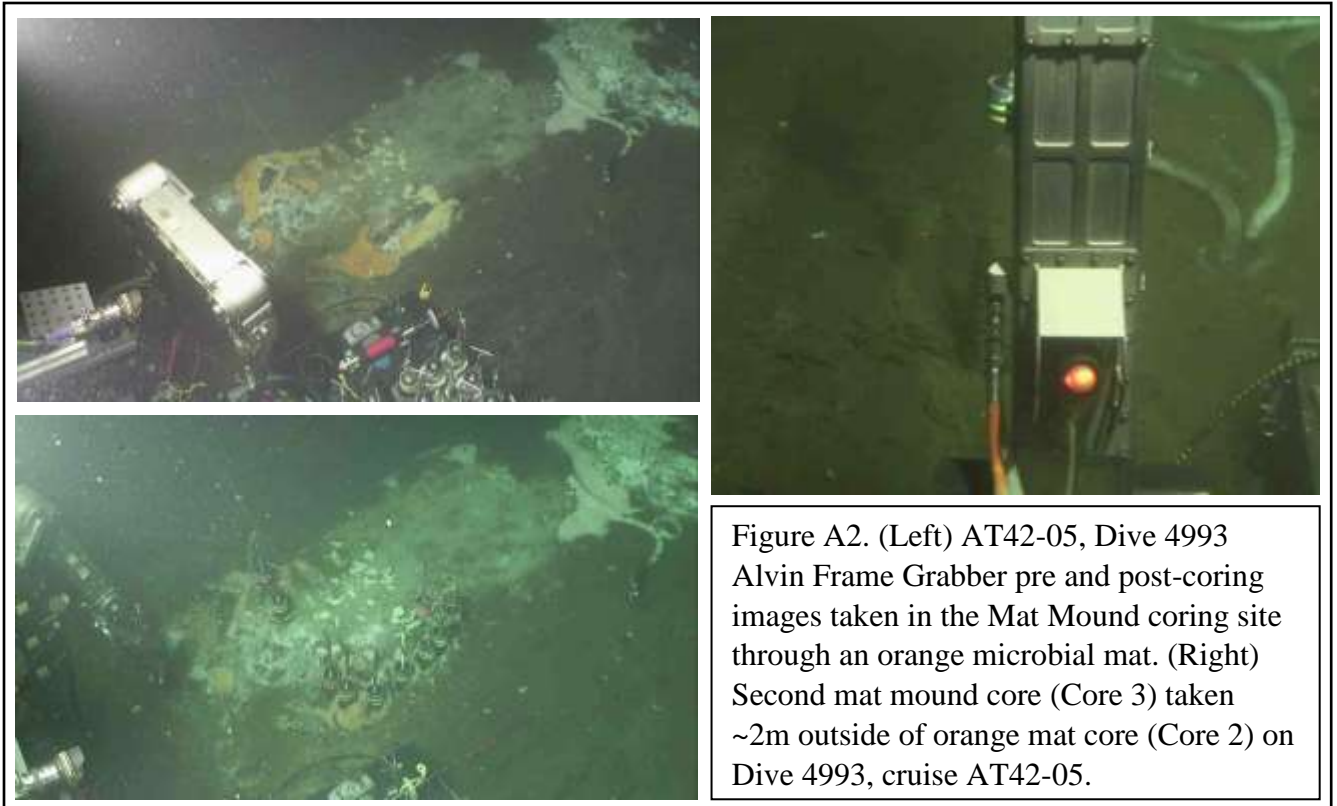| Depth (cmbsf)	Core 1	Core 2	Core 3	Core 4	Core 5	Core 6	Core 7	Core 8	Core 9	Core 10	Core 11	Core 12	Core 13	Core 14	Core 15	Core 16
5	*6.2*	*20.7*	3.1	5	9.0	-	-	-	4.8	4.8	32.7	3.2	13.0	20.6	23.0	-
10	*8.2*	*37.0*	4.1	10.4	16.0	-	-	-	7.1	7.1	36.8	*3.3*	20.0	44.0	53.0	-
15	*10.2*	*47.0*	5.9	-	-	-	-	-	8.7	8.7	44.0	*3.4*	20.0	*59.0*	*66.5*	-
20	*12.3*	*55.7*	8.4	-	-	-	-	-	11.1	11.1	49.4	*3.5*	27.0	74.0	80.0	-
25	*14.3*	*63.7*	11.4	26	41	-	-	-	13.1	13.1	52.8	*3.6*	34.0	-	-	-
30	*16.2*	*73.7*	13.8		-	-	-	-	15.5	15.5	54.5	*3.7*	-	-	-	-
35	*18.0*	*81.3*	15.8	-	-	-	-	-	17.9	17.9	54.6	*3.8*	-	-	-	-
40	*20.3*	*86.0*	18.8	-	-	-	-	-	20.3	20.3	55.0	*3.9*	-	-	-	-
45	*22.3*	*89.5*	20.5		-	-	-	-	22.7	22.7	56.6	3.9	-	-	-	-
50	-	-	-	48	56	-	-	-	-	-	-	-	-	-	-	-
Average Temp:	14.2	61.6	11.3	22.4	30.5	-	-	-	13.5	13.5	48.5	3.6	22.8	49.4	55.6	-
Higher ^{224}Ra Act:	In-Situ	In-Situ	Eq	In-Situ	In-Situ	In-Situ	In-Situ	In-Situ	In-Situ	In-Situ	Eq	Eq	In-Situ	Eq	Eq	Eq
Coring Site:	AB	MM	MM	CH	CH	CH	CH	CH	AB	AB	AB	AB	CH	CH	CH	CH
Mat Type:	In YE	In OG	Out OG	In YE	In OG	In WH	In WH	In WH	In WH	In WH	In OG	REF	In WH	In OG	Out OG	REF
Dominating Flux:	+z	+z	+z	-z	-z	-z	+z	-z	+z	-z	+z	-z	-z	+z	X	X

*Italicized values are estimates averaged from surrounding layers.

CCU Sample ID	Cruise Event #	Vent Site	Drop Latitude	Drop Longitude	Depth (m)	Temperature (ITS90 °C)	Ra-224 (dpm/L)	Unc (dpm/L)
WC 1-1	1.001	Big Pagoda	27° 00.82' N	111° 24.70' W	2006	2.9	0.02	0.00
WC 2-1	1.005	Red Dragon	26° 59.97' N	111° 25.14' W	2005	2.9	0.01	0.01
WC 2-2	1.005	Red Dragon			2000	2.9	0.01	0.00
WC 2-3	1.005	Red Dragon			1995	2.9	0.00	0.00
WC 2-4	1.005	Red Dragon			1985	2.9	0.00	0.00
WC 2-5	1.005	Red Dragon			1960	2.9	0.02	0.00
WC 2-6	1.005	Red Dragon			1900	2.9	0.01	0.00
WC 2-7	1.005	Red Dragon			1610	3.0	0.01	0.00
WC 4-1	3.002	Big Pagoda	27° 00.90' N	111° 24.65' W	1975	4.5	0.03	0.00
WC 4-2	3.002	Big Pagoda			1970	3.0	0.13	0.01
WC 4-3	3.002	Big Pagoda			1965	3.3	0.34	0.02
WC 4-4	3.002	Big Pagoda			1955	3.0	0.11	0.01
WC 4-5	3.002	Big Pagoda			1930	2.9	0.02	0.00
WC 4-6	3.002	Big Pagoda			1880	2.9	0.01	0.00
WC 4-7	3.002	Big Pagoda			1680	3.0	0.00	0.00
WC 4-8	3.002	Big Pagoda			1480	3.2	0.00	0.00
WC 4-9	3.002	Big Pagoda			1080	4.2	0.00	0.00
WC 4-10	3.002	Big Pagoda			880	5.1	0.00	0.00
WC 4-11	3.002	Big Pagoda			680	6.0	0.00	0.00
WC 4-12	3.002	Big Pagoda			480	8.0	0.00	0.00
WC 5-1	5.002	Big Cactus	27° 35.00' N	111° 27.88' W	1475	3.2	0.00	0.00
WC 5-2	5.002	Big Cactus			1480	3.2	0.00	0.00
WC 5-3	5.002	Big Cactus			1530	3.0	0.00	0.00
WC 5-4	5.002	Big Cactus			1555	3.0	0.00	0.00
WC 5-5	5.002	Big Cactus			1575	3.0	0.00	0.00
WC 6-1	6.002	Big Cactus	27° 34.98' N	111° 27.75' W	1200	3.7	0.00	0.00
WC 6-2	6.002	Big Cactus			1300	3.5	0.00	0.00
WC 6-3	6.002	Big Cactus			1400	3.2	0.01	0.00
WC 6-4	6.002	Big Cactus			1510	3.2	0.02	0.00
WC 6-5	6.002	Big Cactus			1560	3.1	0.00	0.00
WC 6-6	6.002	Big Cactus			1585	3.1	0.02	0.00
WC 6-7	6.002	Big Cactus			1605	3.0	0.02	0.00
WC 6-8	6.002	Big Cactus			1610	3.0	0.01	0.00
WC 7-1	7.001	Sonora Margin	27° 34.95' N	111° 27.85' W	100	15.2	0.00	0.00
WC 7-2	7.001	Sonora Margin			225	12.4	0.01	0.00
WC 7-3	7.001	Sonora Margin			400	8.8	0.00	0.00
WC 7-4	7.001	Sonora Margin			600	6.9	0.00	0.00
WC 7-5	7.001	Sonora Margin			800	5.4	0.00	0.00
WC 7-6	7.001	Sonora Margin			1200	3.8	0.00	0.00
WC 7-7	7.001	Sonora Margin			1400	3.3	0.01	0.00
WC 7-8	7.001	Sonora Margin			1479	3.1	0.00	0.00
WC 7-9	7.001	Sonora Margin			1529	3.1	0.00	0.00
WC 7-10	7.001	Sonora Margin			1554	3.0	0.00	0.00
WC 7-11	7.001	Sonora Margin			1574	3.0	0.03	0.00
WC 7-12	7.001	Sonora Margin			1579	3.0	0.00	0.00
WC 8-1	8.001	Alvin Spire	27° 00.75' N	111° 24.27' W	1891	2.9	0.00	0.00
WC 8-2	8.001	Alvin Spire			1941	2.9	0.00	0.00
WC 8-3	8.001	Alvin Spire			1966	2.9	0.01	0.00
WC 8-4	8.001	Alvin Spire			1985	2.9	0.03	0.00
WC 8-5	8.001	Alvin Spire			1991	3.5	0.08	0.01
WC 9-1	10.002	Falkor's Fountain	27° 00.65' N	111° 24.42' W	1878	2.9	0.00	0.00
WC 9-2	10.002	Falkor's Fountain			1928	2.9	0.00	0.00
WC 9-3	10.002	Falkor's Fountain			1953	2.9	0.01	0.00
WC 9-4	10.002	Falkor's Fountain			1973	2.9	0.01	0.00
WC 9-5	10.002	Falkor's Fountain			1978	3.0	0.11	0.01

WC 10-1	11.003	Control	27° 16.46391' N	111° 26. 55857' W	1803	2.6	0.00	0.00
WC 10-2	11.003	Control			1853	2.6	0.00	0.00
WC 10-3	11.003	Control			1878	2.6	0.00	0.00
WC 10-4	11.003	Control			1898	2.6	0.00	0.00
WC 10-5	11.003	Control			1903	2.6	0.01	0.00
WC 11-1	12.003	Texas T Methane	27° 34.94336' N	111° 27.74286' W	1483	3.1	0.01	0.00
WC 11-2	12.003	Texas T Methane			1533	3.1	0.01	0.00
WC 11-3	12.003	Texas T Methane			1558	3.0	0.00	0.00
WC 11-4	12.003	Texas T Methane			1578	3.0	0.02	0.00
WC 11-5	12.003	Texas T Methane			1583	3.0	0.01	0.00
WC 12-1	13.001	Big Pagoda	27° 0.88552' N	111° 24.62873' W	1671	2.9	0.00	0.00
WC 12-2	13.001	Big Pagoda			1921	2.9	0.02	0.00
WC 12-3	13.001	Big Pagoda			1961	3.0	0.01	0.00
WC 12-4	13.001	Big Pagoda			1966	3.9	0.37	0.03
WC 12-5	13.001	Big Pagoda			1971	5.4	0.36	0.03
WC 13-1	14.001	Pescadero	23° 57.413' N	108° 51.722' W	3640	1.9	0.00	0.00
WC 13-2	14.001	Pescadero			3655	2.5	0.19	0.01
WC 13-3	14.001	Pescadero			3659	5.6	1.37	0.10

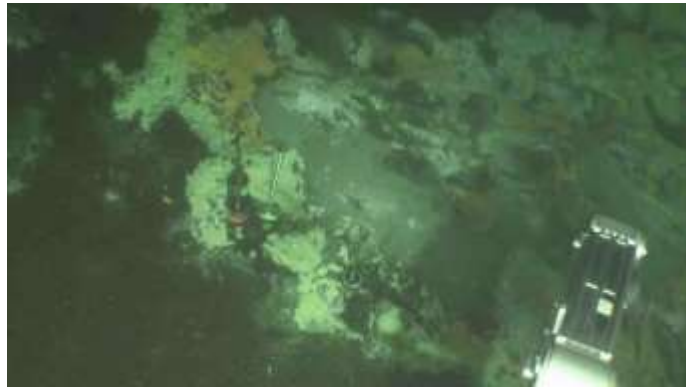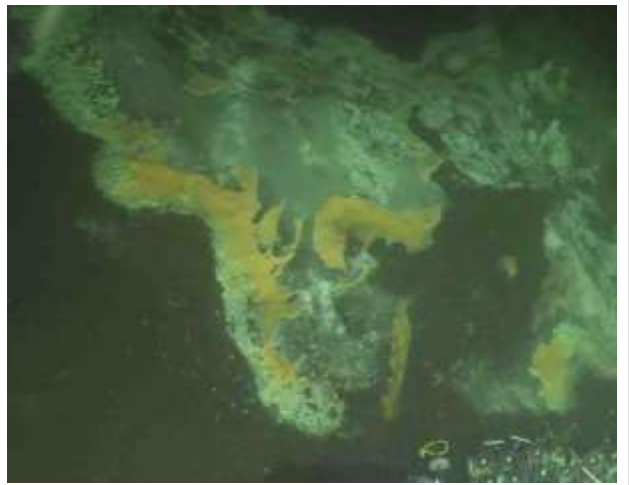# APPENDIX II: Frame-Grabber Coring Images

Figure A1. (Left) AT42-05, Dive 4992 Alvin Frame Grabber images taken in the first Aceto Balsamico coring sites through a yellow microbial mat. (Right) Coring map for Aceto Balsamico map for Dive 4992, based on sketch on the spot in *Alvin*, and checked by the pilot.

Figure A2. (Left) AT42-05, Dive 4993 Alvin Frame Grabber pre and post-coring images taken in the Mat Mound coring site through an orange microbial mat. (Right) Second mat mound core (Core 3) taken ~2m outside of orange mat core (Core 2) on Dive 4993, cruise AT42-05.

Figure A3. (Left) AT42-05, Dive 4994 Alvin Frame Grabber pre and post-coring images of Cores 4, 5 and 6 in Cathedral Hill. (Right) Pre-coring image of yellow, white, and orange microbial mat in Cathedral Hill where Cores 4,5 and 6 were collected.
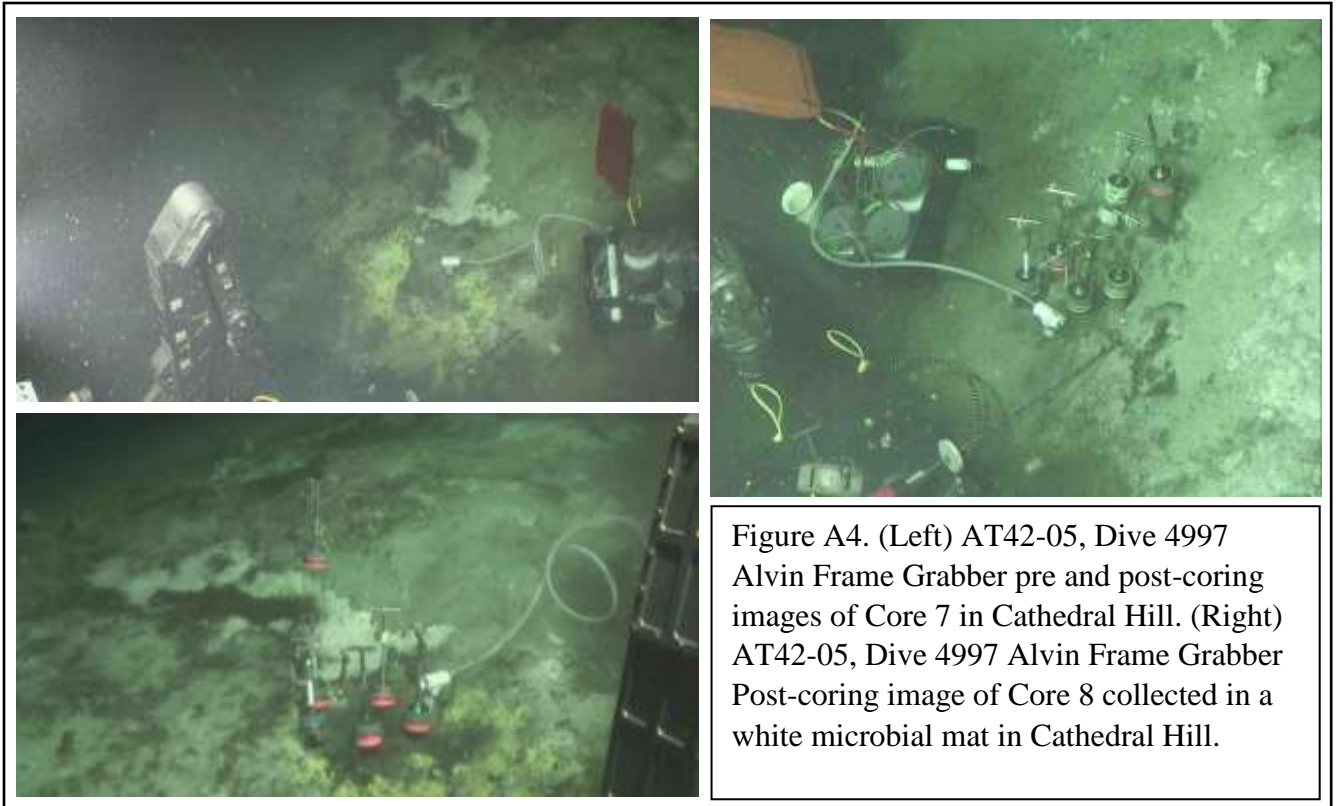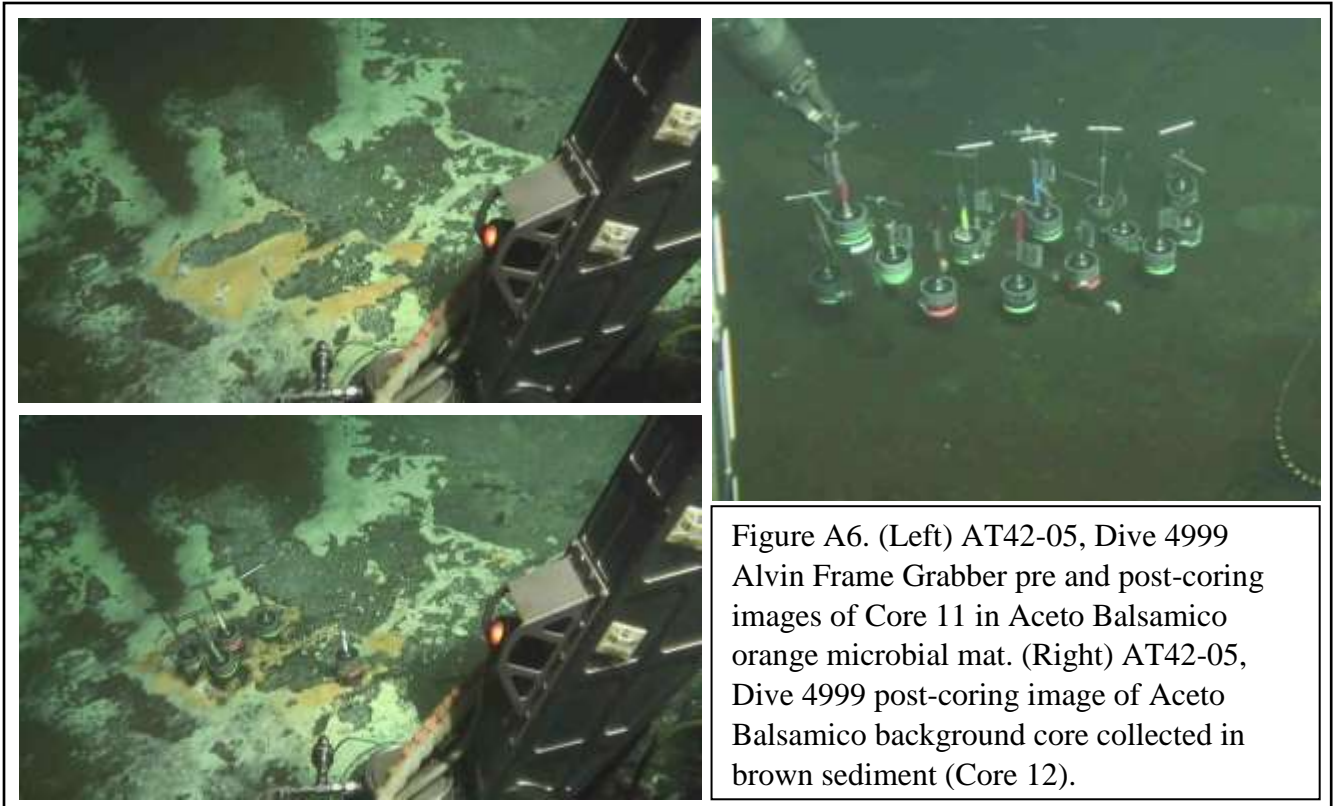
Figure A4. (Left) AT42-05, Dive 4997 Alvin Frame Grabber pre and post-coring images of Core 7 in Cathedral Hill. (Right) AT42-05, Dive 4997 Alvin Frame Grabber Post-coring image of Core 8 collected in a white microbial mat in Cathedral Hill.

Figure A5. (Left) Pre-coring image taken on AT42-05, Dive 4998 white microbial mat in Aceto Balsamico coring site where Cores 9 and 10 were collected.
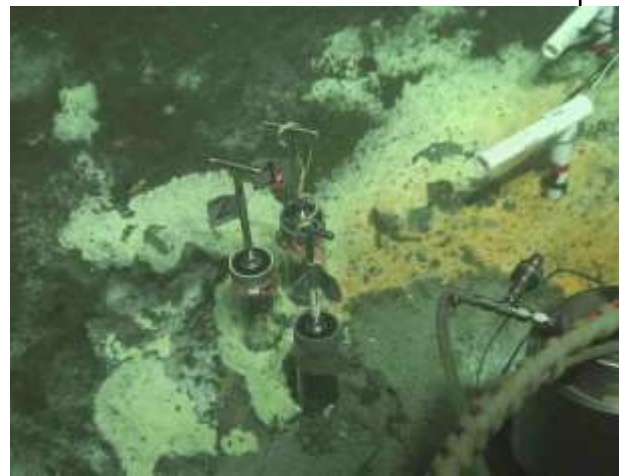
Figure A6. (Left) AT42-05, Dive 4999 Alvin Frame Grabber pre and post-coring images of Core 11 in Aceto Balsamico orange microbial mat. (Right) AT42-05, Dive 4999 post-coring image of Aceto Balsamico background core collected in brown sediment (Core 12).
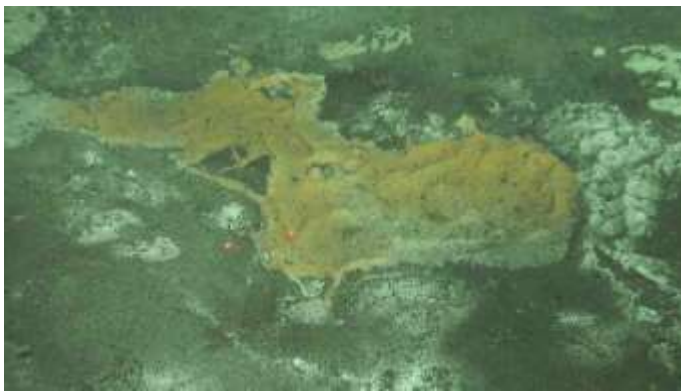
Figure A7. (Left) AT42-05, Dive 5000 Alvin Frame Grabber pre and post-coring images of Cores 14 and 15 in and out of Cathedral Hill orange microbial mat. (Right) AT42-05, Dive 5000 post-coring image of Cathedral Hill core collected in White Microbial mat (Core 13).
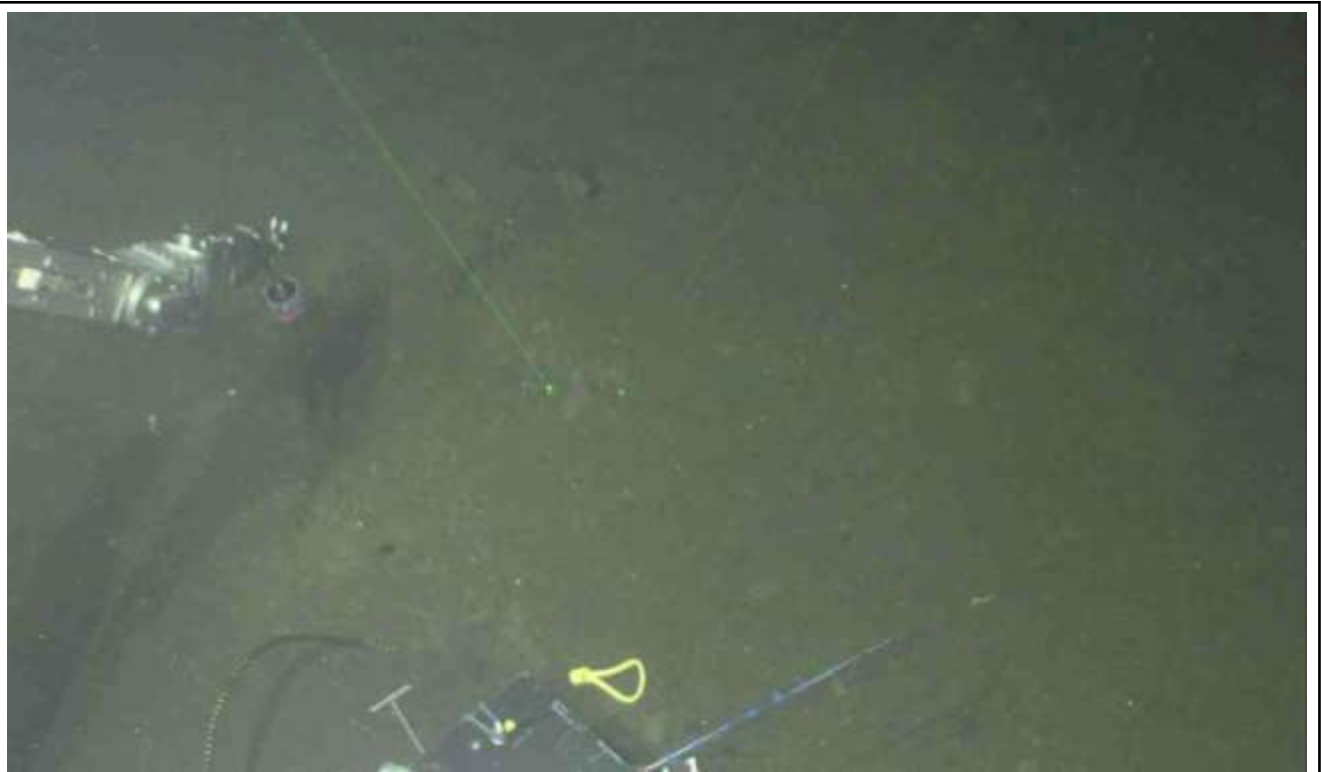
Figure A8. AT42-05, Dive 5001 Alvin Frame Grabber pre-coring image of Cathedral Hill background core collected in brown sediment.